Order Number 9011014

Thermal activation and macroscopic quantum phenomena in superconducting devices

Sharifi, Fred, Ph.D.

University of Illinois at Urbana-Champaign, 1989

U·M·I
300 N. Zeeb Rd.
Ann Arbor, MI 48106

THERMAL ACTIVATION AND MACROSCOPIC QUANTUM PHENOMENA IN SUPERCONDUCTING DEVICES

BY

FRED SHARIFI

B.S., University of Illinois, 1982
M.S., University of Illinois, 1983

THESIS

Submitted in partial fulfillment of the requirements
for the degree of Doctor of Philosophy in Physics
in the Graduate College of the
University of Illinois at Urbana-Champaign, 1989

Urbana, Illinois

UNIVERSITY OF ILLINOIS AT URBANA-CHAMPAIGN

THE GRADUATE COLLEGE

SEPTEMBER 1989

WE HEREBY RECOMMEND THAT THE THESIS BY

FRED SHARIFI

ENTITLED THERMAL ACTIVATION AND MACROSCOPIC QUANTUM PHENOMENA IN SUPERCONDUCTING DEVICES

BE ACCEPTED IN PARTIAL FULFILLMENT OF THE REQUIREMENTS FOR THE DEGREE OF DOCTOR OF PHILOSOPHY

Director of Thesis Research

Head of Department

Committee on Final Examination†

Chairperson

† Required for doctor's degree but not for master's.

O-517

THERMAL ACTIVATION AND MACROSCOPIC QUANTUM PHENOMENA
IN SUPERCONDUCTING DEVICES

Fred Sharifi, Ph.D.
Department of Physics
University of Illinois at Urbana-Champaign, 1989
Dale J. Van Harlingen, Advisor

This thesis is a study of escape from metastable wells in one and two dimensional potentials of superconducting devices. We have measured escape rates due to both thermal activation over the barrier and macroscopic quantum tunneling through the barrier. The measurements were performed for a variety of device parameters, corresponding to different shapes of the potential barrier. We find strong evidence for macroscopic quantum tunneling in both one and two dimensional systems with an escape rate that is very sensitive to the dissipation present in the system. Surprisingly, we have also found a discrepancy between our results and the predictions of Kramers' thermal activation model in certain types of potentials.

ACKNOWLEDGMENTS

This work would never have been possible without the unselfish support and generous help of my thesis advisor, Dale Van Harlingen. Not only have my studies been successful because of his guidance, I have also been fortunate to gain a good friend during these years.

I would also like to thank all my lab mates who have helped me in too many ways to mention: Ron Wakai for sharing his understanding and deep insight of fluctuation effects, Jorge Gavilano and Jonas Zmuidzinaz for their friendly collaboration in various areas, and Kendall Springer for his insane sense of humor which kept the rest of us sane.

Special thanks are due to Gene Hilton who taught me most of what I know technically. I have never met a more giving and unselfish person and I consider it a great priviledge to be his friend; his unique personality and pure heart are rarities. I will miss him greatly.

I wish all of my new lab mates good fortune in the coming years and thank them with putting up with my less desirable characteristics in the past year. I am sure they will all persevere and be successfull in the future.

Finally I would like to thank my family for giving me infinite support and guidance throughout my whole life. I have benefited greatly from their wisdom.

This work was supported by the National Science Foundation through Grants No. NSF-DMR-87-22080 and NSF-DMR-84-11631. The Materials

Research Laboratory also provided microfabrication and cryogenic facilities under National Science Foundation Grant No. NSF-DMR-86-12860. I would also like to thank the University of Illinois for supporting me during the 1988-1989 academic year as a University Fellow.

TABLE OF CONTENTS

Chapter 1

INTRODUCTION

The experimental work presented here was motivated by a fundamental question posed by Leggett regarding quantum mechanics [1,2]. Can one apply quantum theory to macroscopic systems? That is, if one took a macroscopic entity and created a suitable environment in which its classical behavior is suppressed, would it behave quantum mechanically?

In a sense, the question is a reformulation of the debate that the founders of quantum theory engaged in for several years. During those years, the interpretation of a quantum mechanical wave function, and in particular the concept of linear superposition of states, had not been fully developed. If one regards a wave function as a represention of a physical entity and not an abstract mathematical artifact, then a quantum system existing in a superposition of states clearly has some very disturbing implications regarding our accepted notions of reality. The collapse of a wave function into a eigenstate during a measurement process is also not a very satisfying explanation for what is observed. It is comforting to assume that a system, whether macroscopic or microscopic, has an existence all its own with or without a measurement being performed on it. Our understanding of this situation only worsens for macroscopic systems.

Unfortunately, interest in this field has waned considerably,

mainly because of widespread acceptance of Bohr's Copenhagen interpretation. In essence, this interpretation forbids us to ask what quantum measurement theory means rather than define it. Today most physicists use the quantum formalism to solve a variety of problems without giving much thought to these questions. Quantum mechanics has become a recipe that is applied to a particular situation, where some result is obtained. Few physicists, most notably Bell [3], are willing to study this fascinating subject. Familiarity with the use of quantum theory has bred a misleading illusion of its understanding.

One main reason why we are so comfortable with this process is that until very recently quantum mechanics was used only for the microscopic world. For a variety of reasons related to size scales, we are perfectly comfortable with electrons being in a superposition of states. But assuming it is possible to formulate a wave function for a macroscopic system, then can one see quantum effects being exhibited in such a system? That is, we would like to perform an experimental to verify (or disprove) the Schroedinger cat paradox.

It should also be noted that the question is subtle. It is not whether a macroscopic effect can result if quantum mechanics is applied to a microscopic system. For example, superconductivity and magnetism are macroscopic phenomena resulting from applying quantum theory to microscopic systems. Instead we wish to consider a macroscopic system and see whether it obeys quantum theory. Admittedly, the definition of what is considered to be a macroscopic system is by nature rather subjective. However we have chosen a

system such that its macroscopic nature may be reasonably agreed upon.

In order to verify the existence of quantum phenomena in macroscopic systems, it is necessary to search for effects such as tunneling or coherence, where no classical analogy exists. In the case of tunneling, an object trapped in a metastable potential well has a finite lifetime and eventually escapes through the barrier. With quantum coherence, an object will exist simultaneously in both minima of a degenerate double-well potential, with possibly different probability amplitudes for the two wells (Figure 1.1).

There are two closely related points regarding quantum systems and quantum measurement theory that need to be addressed. The first is rather fundamental: a quantum system will not exist in a linear superposition of states if it is being observed. The measurement act will force the system into an eigenstate. One must perform the experiment without directly observing the system. In practice, it is necessary to ensure that the bandwidth of the measuring apparatus is not on the same order of magnitude as the relevant frequencies (or lifetimes) in the system being observed.

The second issue involves dissipation. A macroscopic system interacts with an environment which removes energy from the system. Such "friction" coupling a quantum system and its surroundings will drastically alter the behavior of such a system [4]. Dissipative effects have been the subject of much recent work by quantum theorists.

With present technology, it is possible to look for quantum

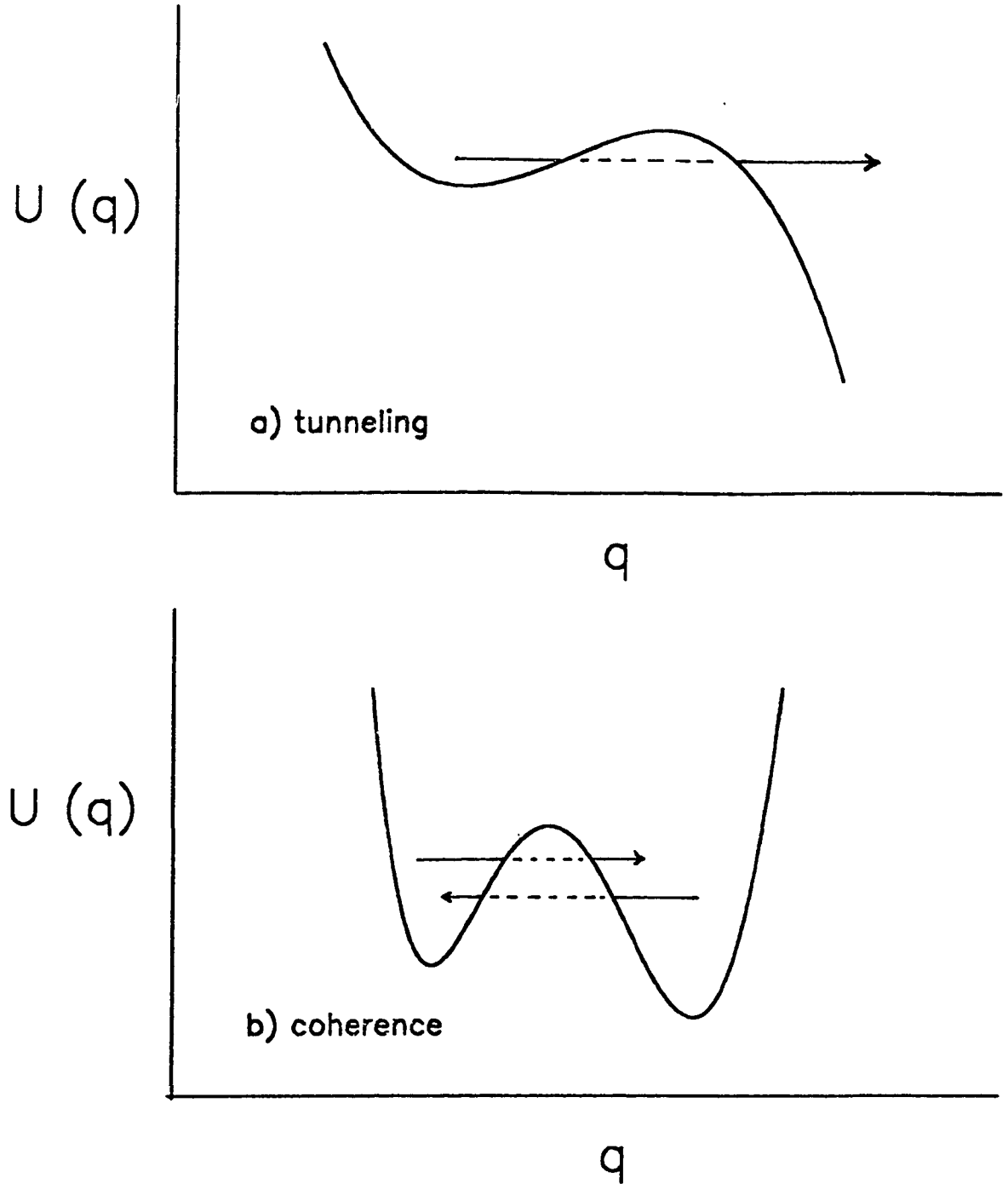

Figure 1.1 - Two forms of potentials that may exhibit quantum behavior: a) tunneling, b) coherence.

effects in macroscopic systems using superconducting devices. Using advanced technology to fabricate small-area, high-quality Josephson junctions, we may study quantum behavior and experimentally construct a system which represents a macroscopic entity trapped in a metastable potential. Such a system will behave quantum mechanically at sufficiently low temperatures and dissipation. It is also possible to externally control the shape of this potential, or even change its dimensionality. In this thesis, we will present various types of tunneling measurements we have performed on Josephson devices. Some novel ideas are also explored with regard to quantum interference in macroscopic systems.

Chapter 2

PHYSICS OF JOSEPHSON DEVICES

The key element in the systems used to perform measurements of macroscopic quantum phenomena consist of Josephson tunnel junctions. Such a device consists of two superconductors separated by a thin insulating barrier about 20Å thick (Figure 2.1). In a conventional superconductor, the distance between the electrons forming Cooper pairs is rather large, being on the order of a few hundred to a few thousand angstroms. Hence, there is considerable overlap between the pairs, causing the pair wave function to lock phase. This results in a pair condensate being formed, where the superconducting wave function, or order parameter, has the same phase value over large distances in the absence of external fields and currents [5,6].

Although an absolute phase cannot be measured, a phase difference can be. In a Josephson device, there is a gauge-invariant phase difference, δ, between the two superconductors across the insulating barrier (Figure 2.1). Since this phase difference describes all of the electrons ($\sim 10^{23}/cm^3$) participating in superconductivity, it is considered to be a macroscopic entity [4]. We have studied the behavior of this macroscopic phase difference in a quantum-mechanical environment.

Josephson showed that although the two superconductors are not in direct contact, Cooper pairs can still tunnel through the insulating barrier [7]. This occurs because the wave function will penetrate

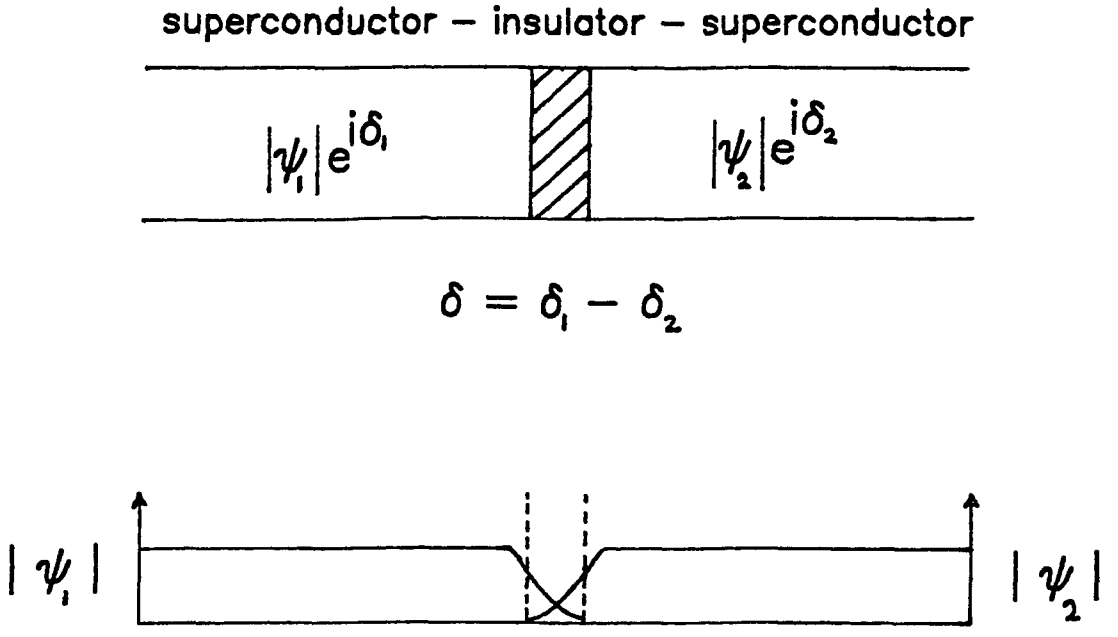

Figure 2.1 - Diagram of a Josephson junction and the magnitude of the superconducting order paramter in such a device.

the barrier with a characteristic decay length dependent on the strength of Cooper pair coupling in the particular superconductor. The coupling energy between the two superconductors is

$$E_c = - \frac{I_c \Phi_o}{2\pi} \cos\delta = - E_j \cos\delta \ . \qquad (2.1)$$

Here Φ_0 is the magnetic flux quantum defined as

$$\Phi_o = \frac{h}{2e} \qquad (2.2)$$

and I_C is the critical current of the junction, the maximum value of the supercurrent that can flow through the junction. The value of the phase difference δ depends on the ratio of the bias current to the critical current,

$$\sin\delta = \frac{I}{I_c} \qquad (2.3)$$

Josephson also showed that the time rate of change of the phase difference is dependent upon the instantaneous voltage across the junction,

$$V = \frac{\Phi_o}{2\pi} \frac{d\delta}{dt} \qquad (2.4)$$

2.1 RSJ Model for a Single Josephson Junction

A more realistic model for a Josephson junction was developed by Stewart [8] and McCumber [9] (Figure 2.2). The resistively-shunted junction (RSJ) model takes into account the finite junction capacitance (due to its size) and also the existence of a normal current along with the supercurrent. The source of this normal current is quasiparticles: the fraction of Cooper pairs broken into normal electrons because of thermal fluctuations at $T > 0$. The total

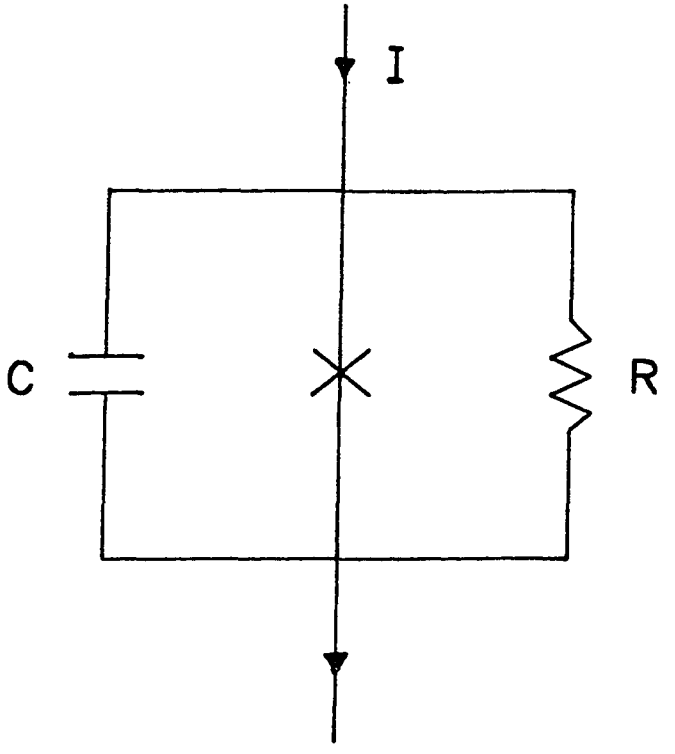

Figure 2.2 - Schematic diagram of the RSJ model for a Josephson junction.

current through the device is divided into the supercurrent, a Maxwell displacement current, and a dissipative normal current,

$$I = I_c \sin\delta + \frac{V}{R} + C\frac{dV}{dt} \tag{2.5}$$

Rewriting using the 2nd Josephson relation, we obtain,

$$I = I_c \sin\delta + \frac{\Phi_o}{2\pi R}\frac{d\delta}{dt} + \frac{C\Phi_o}{2\pi}\frac{d^2\delta}{dt^2} \tag{2.6}$$

This equation represents a damped, driven oscillator with a sinusoidal restoring force (analogous to a driven pendulum) [10]. By combining the force terms, we obtain an expression for the coordinate derivative of a potential,

$$C\left(\frac{\Phi_o}{2\pi}\right)^2\frac{d^2\delta}{dt^2} + \frac{1}{R}\left(\frac{\Phi_o}{2\pi}\right)^2\frac{d\delta}{dt} = -\frac{d}{d\delta}U(\delta) \tag{2.7}$$

where $U(\delta)$ and i are defined as follows:

$$U(\delta) = -2E_J\,[i\delta + \cos\delta] \tag{2.8}$$

$$i = \frac{I}{I_c}\,. \tag{2.9}$$

Thus we obtain a potential for a macroscopic variable whose coordinate is the value of the phase difference, moving in a one-dimensional system with a mass proportional to the junction capacitance. The system is also damped, with the damping coefficient proportional to 1/R (Figure 2.3).

It is instructive to represent the zero and finite voltage state of a Josephson device in terms of this "washboard" potential. Ignoring fluctuation effects for the moment, for values of $0 < i < 1$, the "particle" is trapped in a metastable well. As the bias current

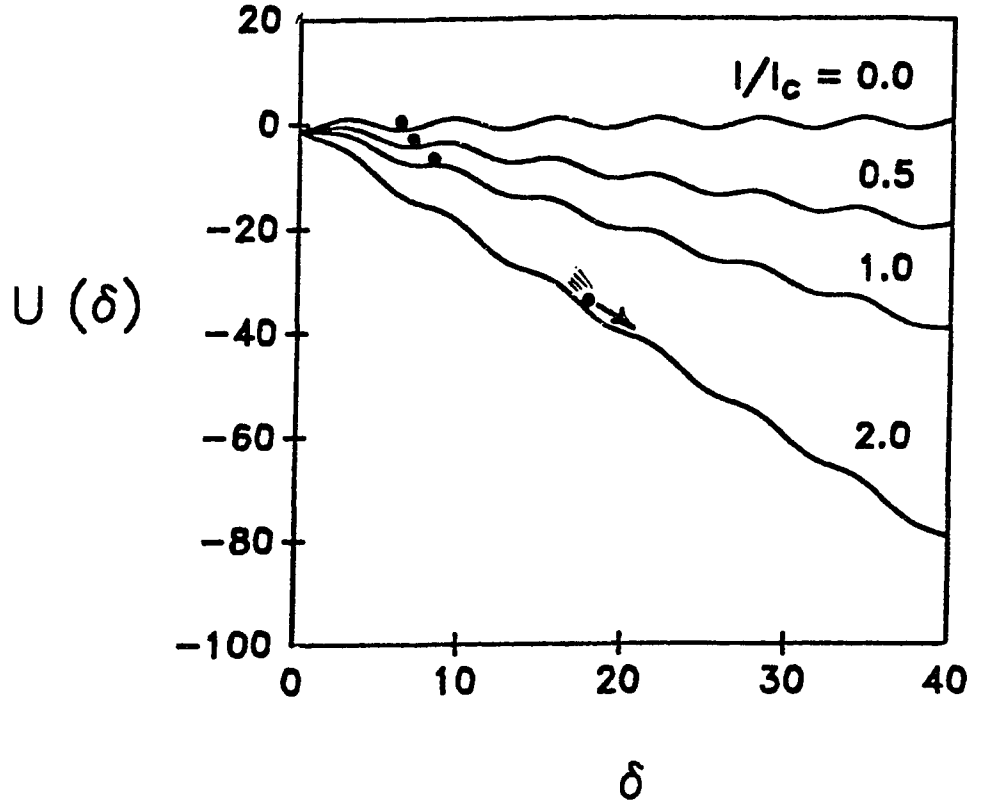

Figure 2.3 - "Washboard" potential of a current-biased Josephson junction for various bias values. The potential axis is represented in units of E_J.

is increased, the barrier height of the well is reduced. Finally at $i = 1$, the metastable well disappears and the local maximum becomes an inflection point. Then the particle is no longer confined and rolls down the washboard potential, causing the time-averaged rate of change of the phase, $< d\delta/dt >$, to be finite. From the second Josephson relation,

$$\langle V \rangle = \frac{\Phi_o}{2\pi} \left\langle \frac{d\delta}{dt} \right\rangle \neq 0 \tag{2.10}$$

and the junction is now in the finite voltage state with a net dc component.

The damping in Josephson junctions is characterized by a dimensionless friction coefficient [11]

$$\beta_c = \frac{2\pi I_c R^2 C}{\Phi_o} . \tag{2.11}$$

If $\beta_C > 1$, the motion is underdamped and the particle will not be retrapped until the bias current is reduced below the point at which escape initially occurred. If $\beta_C < 1$, the system is overdamped and must be driven in order to sustain the evolution of the phase. Figure 2.4 shows the I-V characteristics of a Josephson device for various damping values.

2.2 THE DC SQUID

A more complex device made of Josephson junctions is the dc Superconducting QUantum Interference Device (SQUID). In such a device, two Josephson junctions are connected in parallel in a loop of inductance L (Figure 2.5). Although this system is similar to that of a single junction, it exhibits differences if a magnetic field is

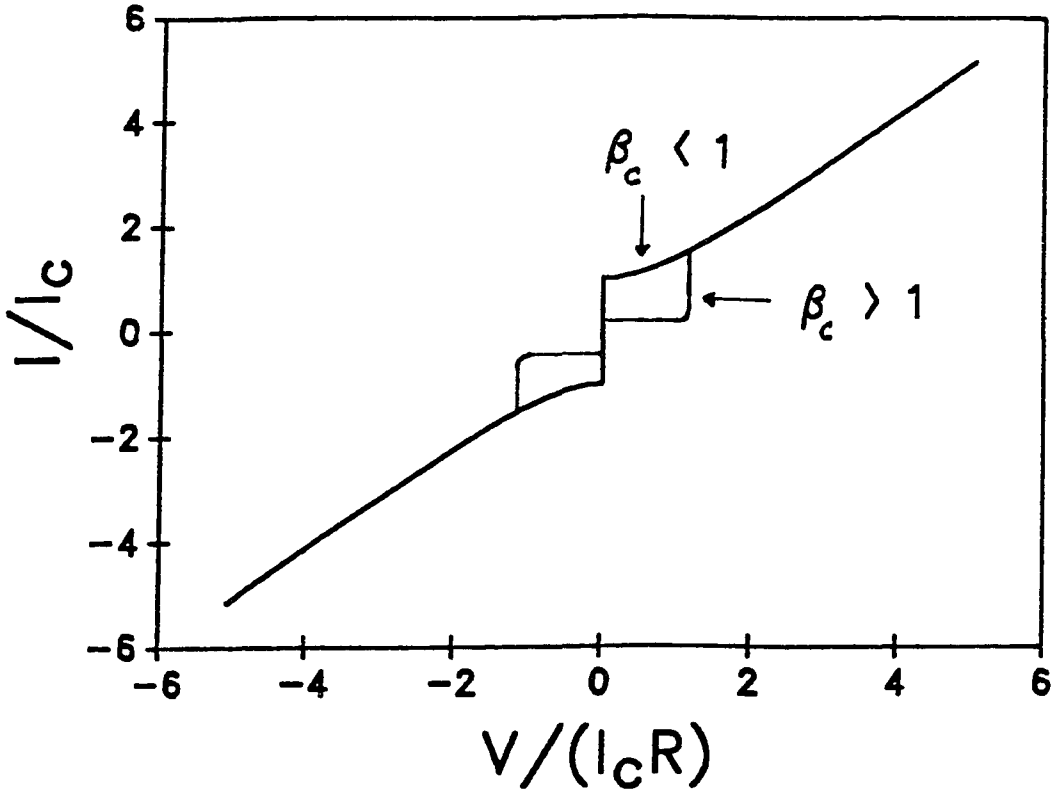

Figure 2.4 - I-V characteristics of a Josephson junction in the underdamped and overdamped regime.

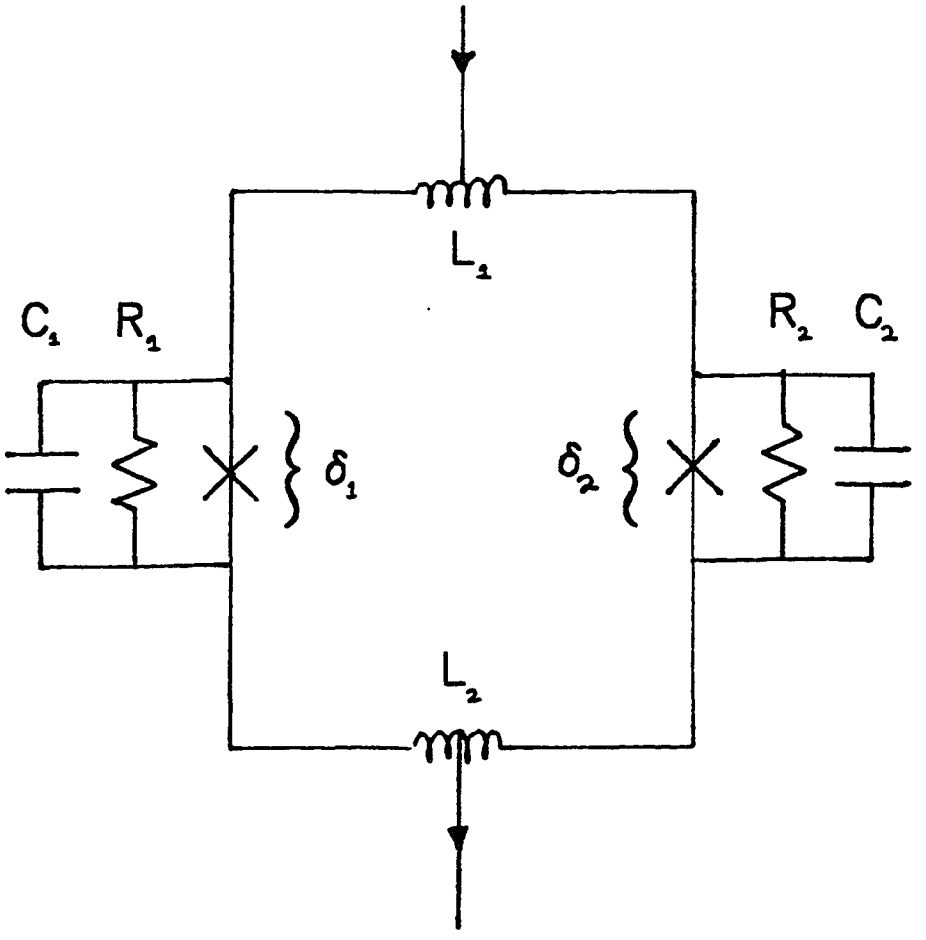

Figure 2.5 - Schematic diagram of a dc SQUID. δ_1 and δ_2 are the phase differences across each junction.

applied through the SQUID loop. In such a case, circulating currents are induced in the loop, which affect the value of the phase differences across the two junctions. The bias current through the loop branches into two parts: I_1 and I_2. In the presence of a magnetic flux, the normalized circulating current term can be written as [12]

$$J = \frac{I_2 - I_1}{2} = \frac{1}{\pi\beta_L}\,[\delta_1 - \delta_2 - 2\pi f] \tag{2.12}$$

Here β_L is the SQUID inductance parameter defined as

$$\beta_L = \frac{2L\,I_c}{\Phi_o} \tag{2.13}$$

and f is the reduced external flux through the loop

$$f = \frac{\Phi_e}{\Phi_o}\,. \tag{2.14}$$

The value of β_L determines the magnitude of the circulating current induced in the loop by the external flux. If the induced circulating current is large, the maximum amount of supercurrent that can be put through the device will be reduced. Figure 2.6 plots the magnitude of the critical current as a function of the applied flux for various values of the SQUID inductance parameter.

Since there are two phase differences in such a system, the potential is two-dimensional. It is expressed as

$$U = U_1 + U_2 + \tfrac{1}{2}\,LJ^2 \tag{2.15}$$

where U_1, U_2 are the individual junction energies and the last term is the magnetic energy stored in the SQUID loop. This potential can become quite complicated for the general case where asymmetries exist in the device parameters; extensive theoretical work has been

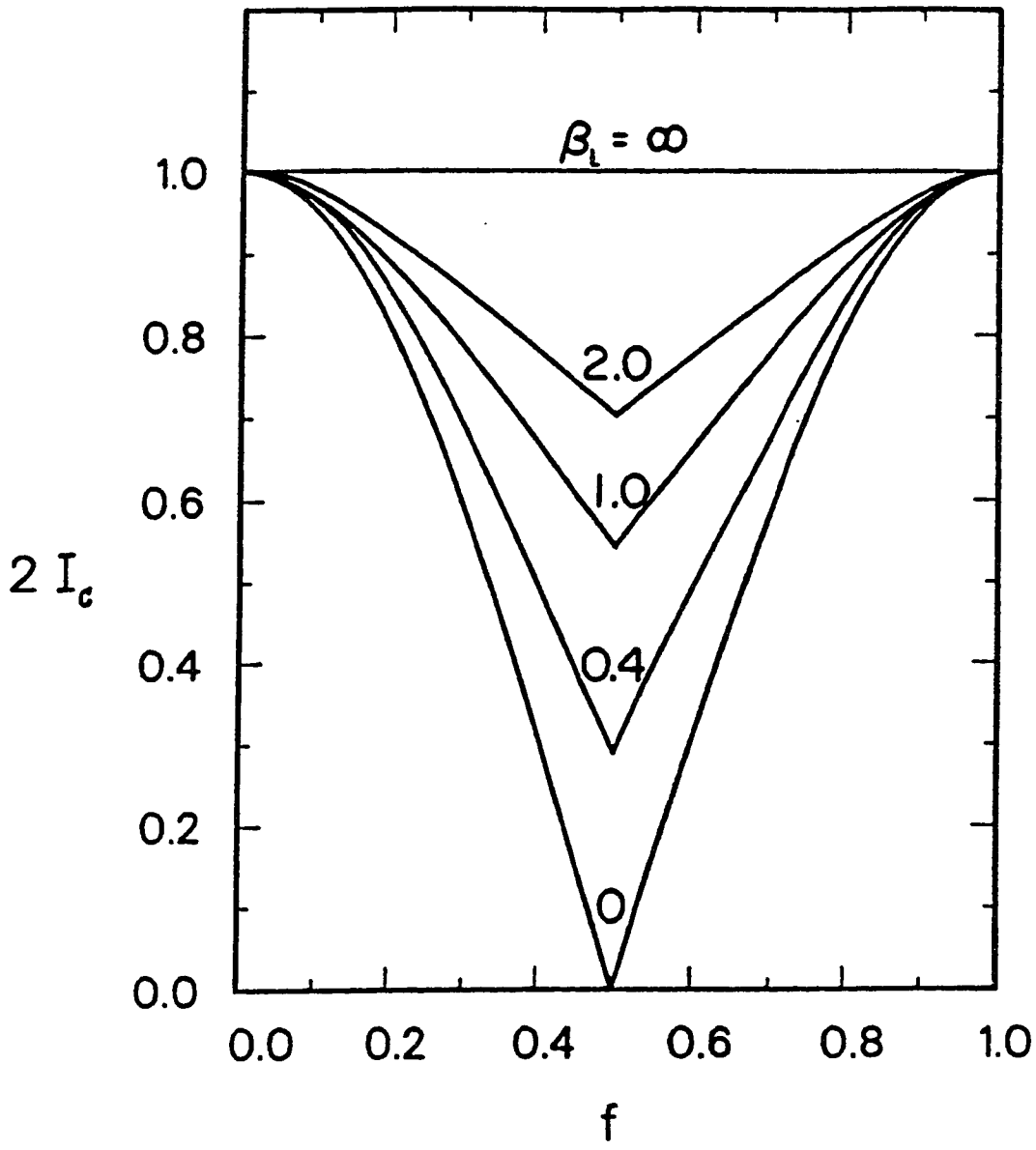

Figure 2.6 - Critical current of a dc SQUID as a function of applied flux for different values of β_L.

done on such systems by Tesche [13]. For the case of a SQUID with inductance symmetry, the potential may be expressed as

$$U(\delta_1, \delta_2) = -E_J \left[(1 - \alpha)\cos(\delta_1) + (1 + \alpha)\cos(\delta_2) + \frac{1}{2}(\delta_1 + \delta_2)i - \frac{1}{2}\pi\beta_L J^2\right] . \quad (2.16)$$

Here α is the asymmetry in the critical currents between the two junctions. Figure 2.7 is a contour plot of these potentials for two values of β_L. As the bias current is increased, the potential is tipped along the line $\delta_1 = \delta_2$. Applying flux shifts the parabolic term of the potential in the δ_1, δ_2 plane and changes the barrier height at a fixed current bias. The dc SQUID is a fascinating and rich system from an experimental point of view because the shape of the potential can be varied greatly through both device parameters and external control biases.

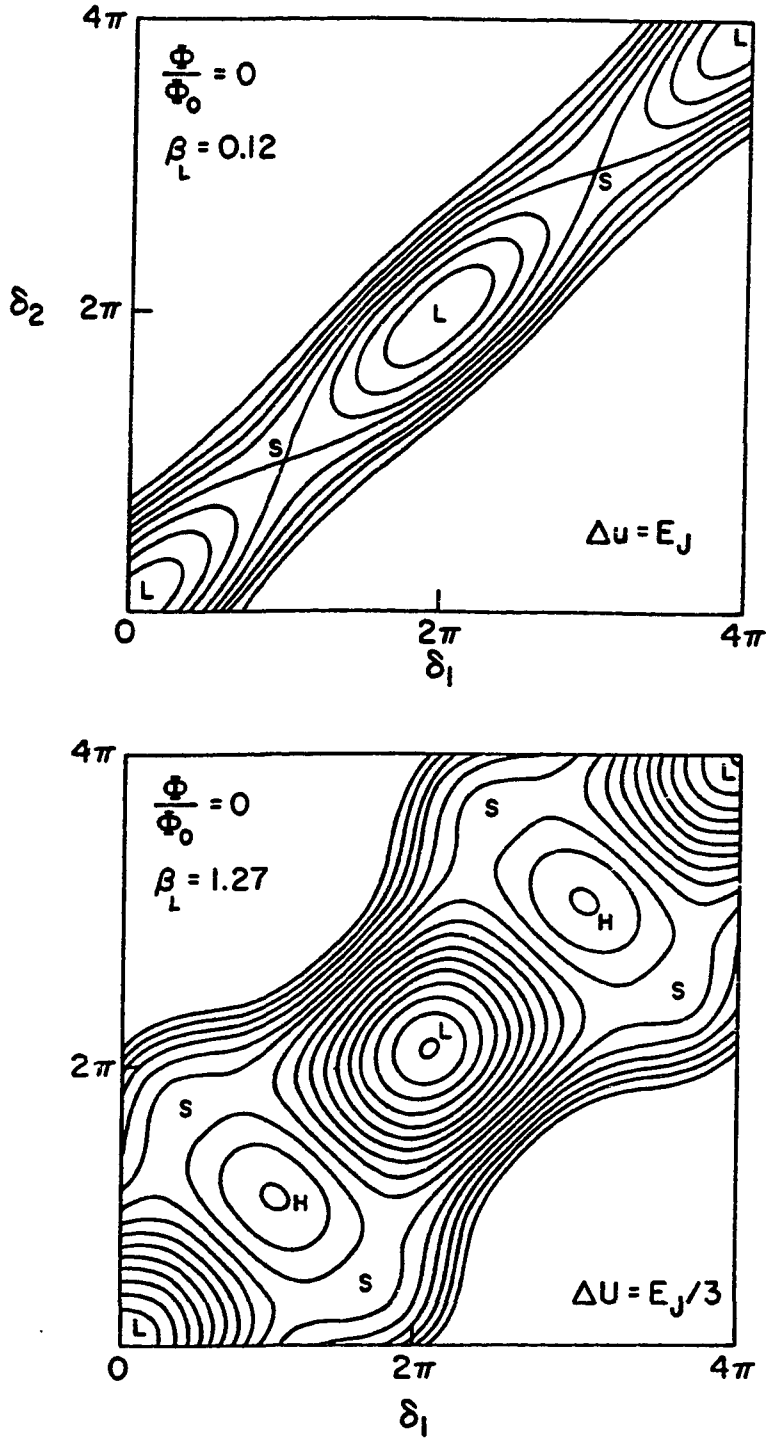

Figure 2.7 - Potential contours of a dc SQUID for two values of the inductance parameter β_L. ΔU is the energy contour spacing.

Chapter 3

FLUCTUATION EFFECTS IN JOSEPHSON DEVICES

In both the dc SQUID and the single junction, in the absence of fluctuations, escape would occur from the local minimum at a barrier height $\Delta U = 0$. However because of fluctuations, escape occurs prematurely at a small but measurable barrier height. That is, as the bias current is increased, there is a jump to the finite voltage state at a bias current slightly smaller than the thermodynamic critical current of the device. Measuring this switching current as a function of temperature (or flux, damping, etc.) yields information regarding the nature of the fluctuation mechanism.

There are two intrinsic fluctuation mechanisms for escape (Figure 3.1). At high temperatures, there is a significant oscillatory normal current due to quasiparticles. These thermal fluctuations induce Johnson noise in the bias current through the junction. In this mode, the escape is classical and occurs over the barrier. There is also the probability of macroscopic quantum tunneling (MQT) through the barrier. As the temperature is lowered, the escape rate due to tunneling will begin to dominate the classical escape rate. There is a crossover temperature, referred to unfortunately as T_c, below which quantum tunneling becomes the dominant escape mechanism.

In the next section, both escape modes are discussed within the framework of Josephson devices. The role that dissipation plays in each case and the interaction between these two mechanisms near the

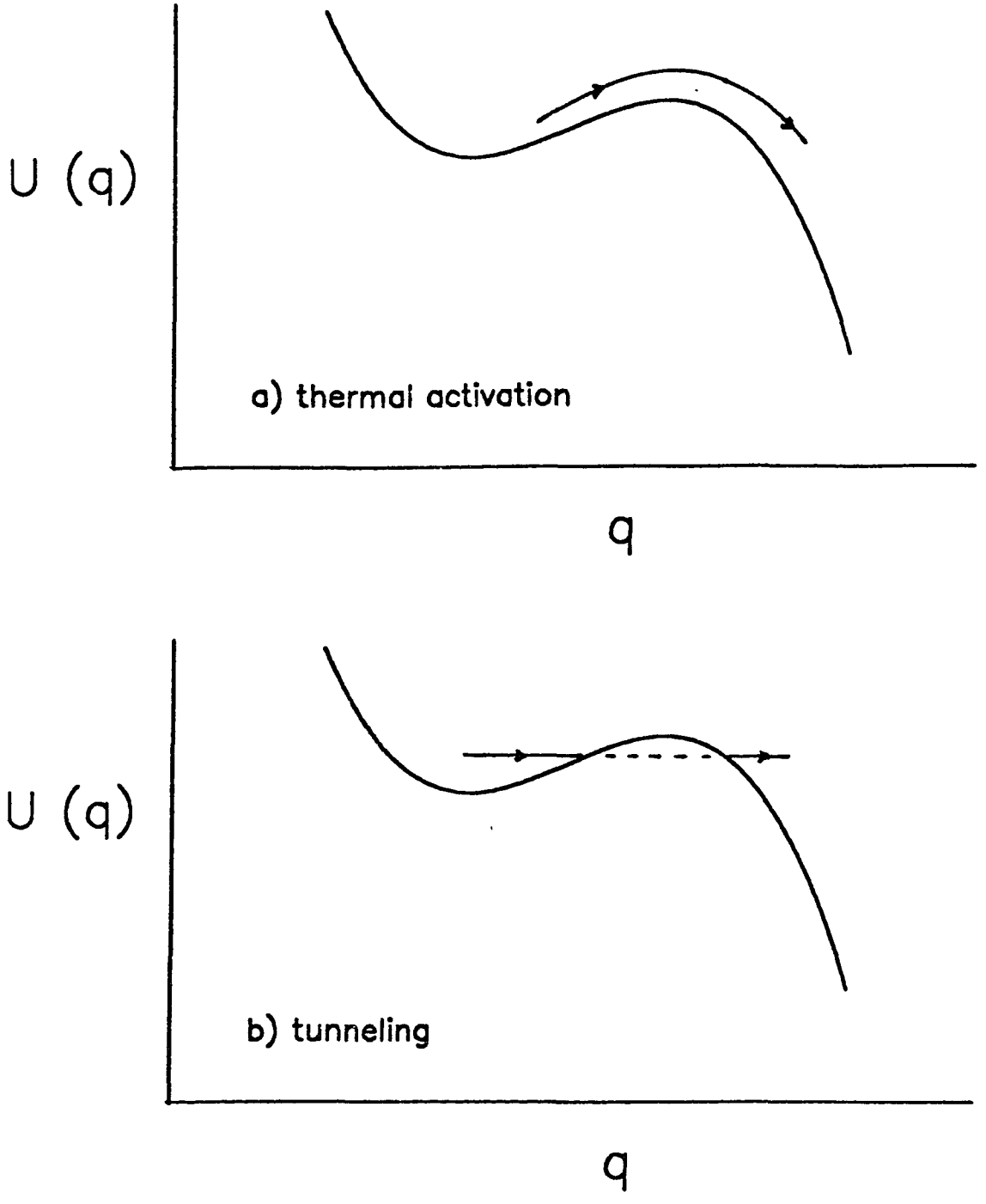

Figure 3.1 - Two mechanisms of escape from a metastable potential well: a) thermal activation, b) quantum tunneling.

crossover temperature is also addressed.

3.1 Classical Escape

The pioneering theoretical work in the area of classical escape from a metastable well was performed by Kramers [14]. In this paper, Kramers studied the behavior of a particle trapped in a metastable potential well undergoing Brownian motion in a viscous environment. Because of the random nature of Brownian motion, the particle will eventually escape over the barrier height through this process. Kramers' calculation of the escape rate is based on a diffusion equation for a distribution of particles trapped in the well where the energy distribution of the particles is determined from the temperature. The escape rate obtained is of the form

$$\Gamma_T = a \frac{\omega_p}{2\pi} \exp(\frac{-\Delta U}{kT}) \ . \qquad (3.1)$$

Here ω_p represents the frequency of small oscillations at the local minimum of the potential well; ΔU is the barrier height of the potential. The prefactor in the above expression can be regarded as an attempt frequency while the exponential part is an Arrhenius factor that determines the probability of escape. It should be noted that this relationship assumes that $\Delta U >> kT$. The factor a is dependent upon the magnitude of the damping in the system.

Some interesting physics is this problem is contained in the prefactor a, and there has been much controversy over the value of this factor in the various damping limits. In general, there is some agreement in the intermediate and strong damping case and less so for the extreme underdamped limit. For the intermediate damping case, a

is of the form [15]

$$a = [(\eta^2/4 + 1)^{\frac{1}{2}} - \eta/2] \tag{3.2}$$

where

$$\eta = \frac{1}{\omega_b RC} \tag{3.3}$$

and ω_b is the magnitude of the (negative) curvature at the top of the barrier. In the strong damping limit, the prefactor becomes [15]

$$a = \omega_b RC \ . \tag{3.4}$$

The case of very weak damping is less clear. If the coupling between the heat bath and the particle is ignored, transition-state theory [16] predicts that the factor a = 1. However a calculation performed by Buttiker [15] within the Kramers' framework, predicts that the prefactor will become extremely small in such a limit. A simplistic physical explanation of this process is to regard an extremely under-damped particle as having a very small resonance width. Thus it would not be able to easily couple to the thermal bath and hence the resultant attempt frequency would be zero. In fact recent experimental evidence in this damping limit suggests that the predictions of transition-state theory are incorrect, and verify Kramers' calculational methods [17]. Various authors have also performed numerical calculations over the complete damping regime [18]. These calculations do agree with the analytic results over certain ranges, though the issue is still far from settled. In such an underdamped limit, there may even be the possibility of exotic non-linear behavior leading to a modification of the Arrhenius factor [19].

Although Kramers' paper deals with the one-dimensional case, its extension to the multi-dimensional problem is straight-forward. In 1955, Brinkman [20] studied the problem of the Brownian motion of a particle in an N-dimensional potential where he obtained expressions that are similar to those of Kramers but are adjusted to include the effect of the additional dimensions,

$$\Gamma_T = \left(\Pi_i \frac{a_i\ \omega_i^m}{\omega_j^s}\right) \exp(-\Delta U/kT) \tag{3.5}$$

Here $j = i + 1$, the subscripts s and m refer to curvatures of the potential at the saddle points and local minima respectively, and the product is over the number of dimensions in the potential.

There is subtle difference between the two cases however. In a multi-dimensional potential, there exists the possibility of more than one escape path. In such a case, the total escape rate is approximately the sum of escape rates through each path.

Besides Josephson junction dynamics, this work has relevance to numerous other fields as well. For example, it is extremely important in the theory of chemical reactions and is used to model reaction rates. However, some problems arise in such applications from the uncertainty in the parameters of the model. For example, it is difficult to ascertain exactly what the barrier height, or attempt frequency is for particular molecules.

On the other hand, Josephson devices can be well modelled using Kramers' formalism. The barrier heights and attempt frequencies depend on circuit parameters such as the bias current or the capacitance. In general, these quantities can be measured with

excellent precision.

Kramers' model is applied to the case of a single junction with critical current I_c and capacitance C by Buttiker [15]. In this system, the curvature (frequency of small oscillations) at the local minimum is equal in magnitude to the (negative) curvature at the top of the well. This plasma frequency is the second derivative of the potential evaluated at the local minimum and is dependent on the bias current:

$$\omega_p = \omega_J \, (1 - i^2)^{\frac{1}{4}} \tag{3.6}$$

where

$$\omega_J = \left(\frac{2\pi I_c}{C\Phi_o}\right)^{\frac{1}{2}} . \tag{3.7}$$

Near i = 1, where escape transitions occur, the barrier height is approximately equal to

$$\Delta U = 2E_J \, [(1 - i^2)^{\frac{1}{2}} - i \arccos(i)] . \tag{3.8}$$

In terms of these parameters, the escape rate expression for a single junction can be determined in the intermediate damping limit by using equation (3.1).

Ben-Jacob [21] has extended this work to the two-dimensional potential of a dc SQUID. Here there are two relevant frequencies at each extrema since the potential is two dimensional. Expressions for these frequencies have been calculated by Tesche [22] in terms of the device parameters. Expressed in normal coordinates of the potential, the frequencies ω_a along and ω_n orthogonal to the escape paths are given by

$$\omega_a^2 = (1 - \alpha)\cos\delta_1\cos^2\epsilon + (1 + \alpha)\cos\delta_2\sin^2\epsilon + \left(\frac{1}{\pi\beta_L}\right)[1 + 2\sin\epsilon\cos\epsilon] \tag{3.9}$$

$$\omega_n^2 = (1 - \alpha)\cos\delta_1\sin^2\epsilon + (1 + \alpha)\cos\delta_2\cos^2\epsilon + \left(\frac{1}{\pi\beta_L}\right)[1 - 2\sin\epsilon\cos\epsilon] \tag{3.10}$$

where

$$\tan\epsilon = \frac{\gamma}{2} + \left(\frac{\gamma^2}{4} + 1\right)^{\frac{1}{2}} \tag{3.11}$$

and γ is defined by the following relationship:

$$\frac{\gamma}{\pi\beta_L} = (1 + \alpha)\cos\delta_2 - (1 - \alpha)\cos\delta_1 \ . \tag{3.12}$$

Equations (3.9) and (3.10) are valid for determining curvatures at local minima, maxima, and saddle points, depending on the value of the coordinates δ_1 and δ_2. The escape rate is then determined from equation (3.5) and the above expressions for the frequencies.

If the potential has more than one saddle point for each local minimum, then the total escape rate is the sum of the rates through each saddle [23]:

$$\Gamma = \Sigma_i \ \Gamma_i \ . \tag{3.13}$$

3.2 Quantum Escape

There is another form of escape possible from a metastable well: quantum tunneling through the barrier. There is always a finite probability of tunneling and as the temperature is lowered the quantum escape rate will eventually become larger than the classical escape rate. This quantum rate will not only depend on the barrier height (as in the classical case) but also on the barrier width.

Although it is possible to write a general formula for escape from a metastable well in an arbitrary potential, it is more instructive to treat a few specific cases. The following discussion ignores damping effects for the moment.

In a high current density ($\sim 10^3$ A/cm^2) Josephson device, escape will not occur until the bias current is close to the critical current of the junction. In such a case, the sinusoidal term of the "washboard" potential expression in equation (2.8) can be accurately approximated by a quadratic minus a cubic term in the phase. Using such an approximation, a WKB method is used to obtain an expression for the escape rate in the zero-temperature limit [24]:

$$\Gamma_q = \left(\frac{7.2\Delta U}{\hbar\omega_p}\right)^{\frac{1}{2}} \frac{\omega_p}{2\pi} \exp\left(\frac{-7.2\Delta U}{\hbar\omega_p}\right) . \qquad (3.14)$$

This expression is derived assuming the particle is in the lowest energy state in the well; in this T = 0 calculation, escapes from the higher levels not considered. The numerical factors arise from the shape of the potential.

By comparing equations (3.1) and (3.14), we can see that the quantum rate will begin to dominate the classical rate at a crossover temperature T_c, approximately given by

$$T_c = \frac{\hbar\omega_p}{7K} . \qquad (3.15)$$

For our devices, plasma frequencies range from 10 GHz to 500 GHz, yielding crossover temperatures on the order of 0.1 to 0.5 K, although we have observed MQT effects at temperatures as high as 2 K. Since the expression for the quantum escape rate is independent of temperature, the signature for MQT occurring is a temperature below

which the escape rate remains constant.

This work is extended to a general multi-dimensional potential by Schmidt [25] who also used a WKB formalism. The expressions he obtains are quite general and are not easily put in the framework of Josephson devices. However, Chen [26] has calculated the quantum escape rate for the specific case of a low β_L dc SQUID (Figure 2.7) where he finds that in this limit the resulting rate is similar to that of a single junction. This resulted is to be expected from the shape of this potential. Since the potential is confined in the direction orthogonal to the escape path, it is similar to that of a one dimensional system. A rate calculation for a dc SQUID with arbitrary parameters can be calculated numerically using path integral techniques.

The existence of a macroscopic entity obeying quantum mechanics was first observed in experiments performed by Voss [27] and later in a series of elegant experiments performed by Clarke's group [28], [29], [30]. Not only did these experiments prove the existence of MQT in a one-dimensional potential, they also verified the quantization of energy levels in the potential well.

3.3 Dissipation

The issue of dissipation is extremely important in the quantum tunneling problem. Since our quantum variable is macroscopic, it will interact with an environment that irreversibly removes energy from the system. The question is how this dissipative environment alters the quantum mechanical escape rate.

Leggett and Caldeira (L-C) [4,31] have attempted to answer this question by forming a model for the dissipation. Briefly, the environment is represented as a bath of harmonic oscillators coupled to the quantum system. The energy removed from the system depends on the number of oscillators that are engaged at any one time. Although the excitations of each oscillator is limited to the first excited state, it is possible to get very strong damping from this model. The damping is also assumed to be ohmic; there is no frequency dependence to R. Using this model, it is found that the quantum escape rate is reduced by dissipation. The suppression is of the form

$$\Gamma = \kappa \left(\frac{7.2\Delta U}{\hbar\omega_p}\right)^{\frac{1}{2}} \left(\frac{\omega_p}{2\pi}\right) \exp\left(\frac{-s\Delta U}{\hbar\omega_p}\right) . \tag{3.16}$$

In the zero-temperature limit and for weak damping the factors κ and s assume the form [31]

$$\kappa = (120\pi)^{\frac{1}{2}} \tag{3.17}$$

$$s = 7.2 \left(1 + \frac{0.87}{\omega_p RC}\right) . \tag{3.18}$$

Numerical methods have to be used to calculate κ and s for arbitrary damping and temperature [32,33].

A manner in which this process can be understood is to regard the dissipative environment as performing observations on the quantum wave function [31]. Such observations occur on a time scale proportional to RC and result in collapsing the wave-packet into an eigenstate, thereby reducing its size (Figure 3.2). By inhibiting the quantum mechanical nature of the system, the tunneling rate is

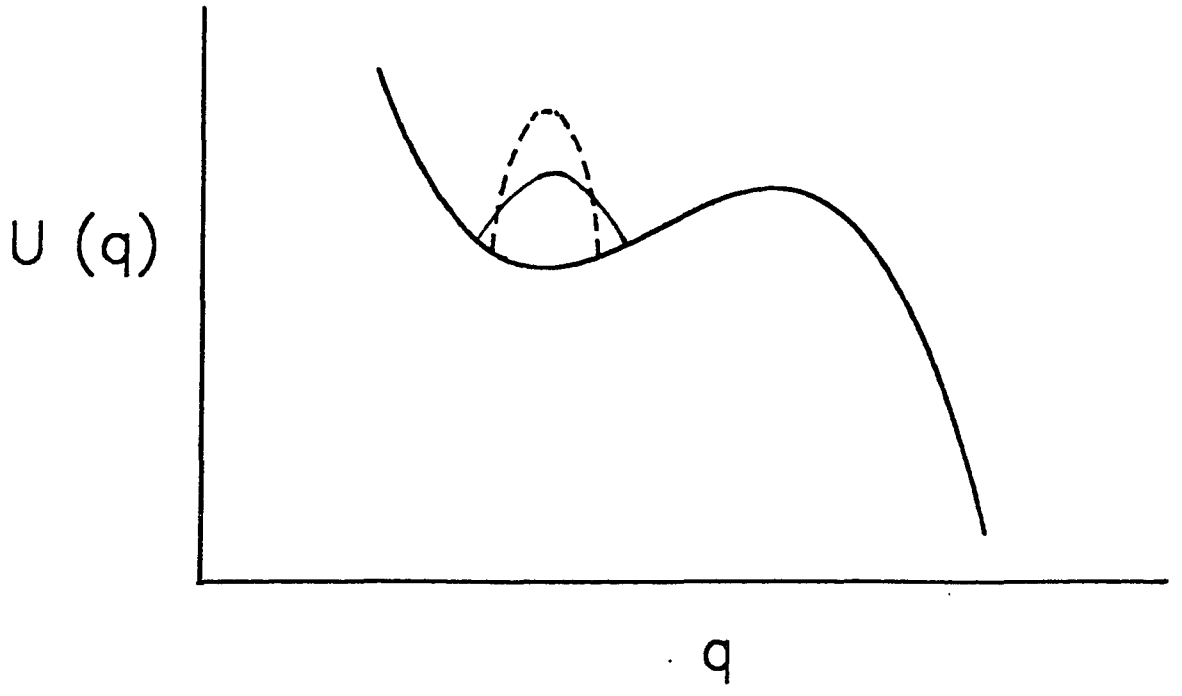

Figure 3.2 - Effect of dissipation (dashed line) on the size of the wavepacket.

reduced.

Equation (3.16) has been verified experimentally by a number of authors [27], [34]. There is general agreement that dissipation does indeed reduce the tunneling rate and suppress the quantum behavior of the system. There is much less agreement over what exactly is the nature of the dissipative mechanism. Two points that need to be addressed is that the L-C model treats R as a frequency-independent parameter, which may or may not be accurate. It is also not obvious to what voltage in the junction I-V this dynamic resistance is relevant.

The experiments performed so far to study the damping mechanism fall into two categories: shunted and unshunted junctions. In the case of shunted junctions, a Josephson device is connected in parallel to a thin film resistor of known resistance value. This resistance is usually lower than any dynamic resistance in the device and dominates the damping. It is also fair to assume that the resistance of this film will be independent of frequency up to a range that includes the plasma frequency of the device. In such cases, the agreement between theory and experiment is remarkable, verifying the L-C model for dissipation [34].

The situation is less clear for the case of unshunted junctions. In the zero-voltage state, the oscillations of the phase at the bottom of the metastable wells are damped by a resistance corresponding to the sub-gap resistance. Thus it is logical to assume that the damping in unshunted junctions would correspond to the sub-gap resistance. However, in all of the experiments performed

so far on unshunted junctions [27], [35], including our measurements, the damping is much larger, yielding a value closer to the normal state resistance. This result is rather surprising, indicating that there may be other factors enhancing the dissipation besides quasiparticles. This discrepancy is rather important because of its implications for future work on macroscopic quantum coherence.

Recently Chen [36] tried to clarify this problem by calculating that the relevant resistance is related to the dynamic resistance of the device at the point in which the junction returns from the finite voltage state to the zero-voltage state. We and other groups [37] have recorded return-voltage measurements in order to verify Chen's calculations. The data is currently being analyzed. We have also devised a way to experimentally vary the resistance of a single Josephson junction in-situ, in an effort to shed more light on this problem. These measurements will be discussed in the later chapters.

3.4 Enhancement of the Escape Rate Near Tc

Near the crossover temperature, there is an enhancement of the escape rate because of interaction between the two escape methods. This subject has been the focus of much work by Grabert and others [38], [39].In their calculations, they have considered the effects of finite temperature on the quantum escape rate and the effect of quantum tunneling on the thermal escape rate.

The enhancement is caused by the following factor. In the quantum regime, there is an escape probability from the excited states in the well. The population density of the higher wells may be significant,

depending on the damping and temperature. In such a case, the tunneling escape rate would be larger from an excited level because of the smaller barrier height and width.

Above the crossover temperature, there is also an enhancement of the rate in the thermal regime due to quantum-mechanical factors. These quantum corrections to the thermal activation model arise when a thermal activation event kicks the particle only part-way up the barrier. Such an event would produce no thermal escape, but there is an appreciable chance of tunneling through the remaining part of the barrier.

Analytic expressions can be obtained only in certain limits for these effects. For the general case, the correction factors, have to be evaluated numerically. These enhancements will produce a "rounding" of the escape rate between the two regimes and have been experimentally observed by us and other groups [40].

Chapter 4

THE JOY OF FABRICATION

In order to see quantum fluctuation effects, it is necessary to fabricate small-area, high current density Josephson devices. Unfortunately, with stringent limits placed on the size and quality of the devices, fabrication often becomes more of an art than a science. The process can become frustrating and the yields rather low. In fact, a protracted slump can test the true spirit and inner fortitude of a device physicist.

The processing methods used in making superconductor devices are in general quite similar to those in the semiconductor industry. Initially, a pattern of the device is made by using a photoresist stencil. The appropriate metal or insulator is then deposited, followed by a solvent soak that removes the stencil. The steps can then be repeated to obtain the desired structure.

This chapter will try to describe in some detail the above methods and their nuances. A caveat for readers trying to reproduce this work is that all of these results are dependent to some degree on various intangibles. These range from the characteristics of the deposition systems to the environmental conditions of the cleanroom. These process descriptions should be regarded as initial conditions only.

4.1 Photoresist Processing

Before photoresist can be fabricated into a stencil, the substrate must first be carefully prepared and must be void of any foreign substances such as dirt or grease. Cleaning usually involves scrubbing the substrate with an Alconox soap solution followed by a de-ionized water rinse. This is followed by ultrasonic cleaning for a few minutes in acetone and isopropanol. The substrate is again rinsed in de-ionized water, blown dry with nitrogen gas, and baked at 120 °C for at least 20 minutes to remove all moisture. Immediately prior to spinning on the photoresist, the substrate may be treated with hexa-methyl disilizane (HMDS) vapor for ten minutes to improve the resist adhesion.

Photoresist is a liquid made of long-chained polymers contained in a solvent solution, usually consisting of xylene. After the substrate has been spin-coated with the resist, it is baked to remove the solvent and harden the resist. The resulting coating is then patterned by exposing selected areas to an ultraviolet (U-V) source or an electron beam (Figure 4.1). In a U-V exposure, a mask is used to define the area to be exposed. This mask is a glass plate coated with a metal (usually Cr) in which a pattern has been etched. In electron beam lithography the pattern is formed by controlling the path of the beam. For positive resists the exposure, whether by U-V or electron beam, results in the polymer chain being broken. The coating is then dipped into a developer solution that removes the exposed resist, leaving a patterned substrate. For negative resists, the exposure cross-links the polymer chains, preventing them from

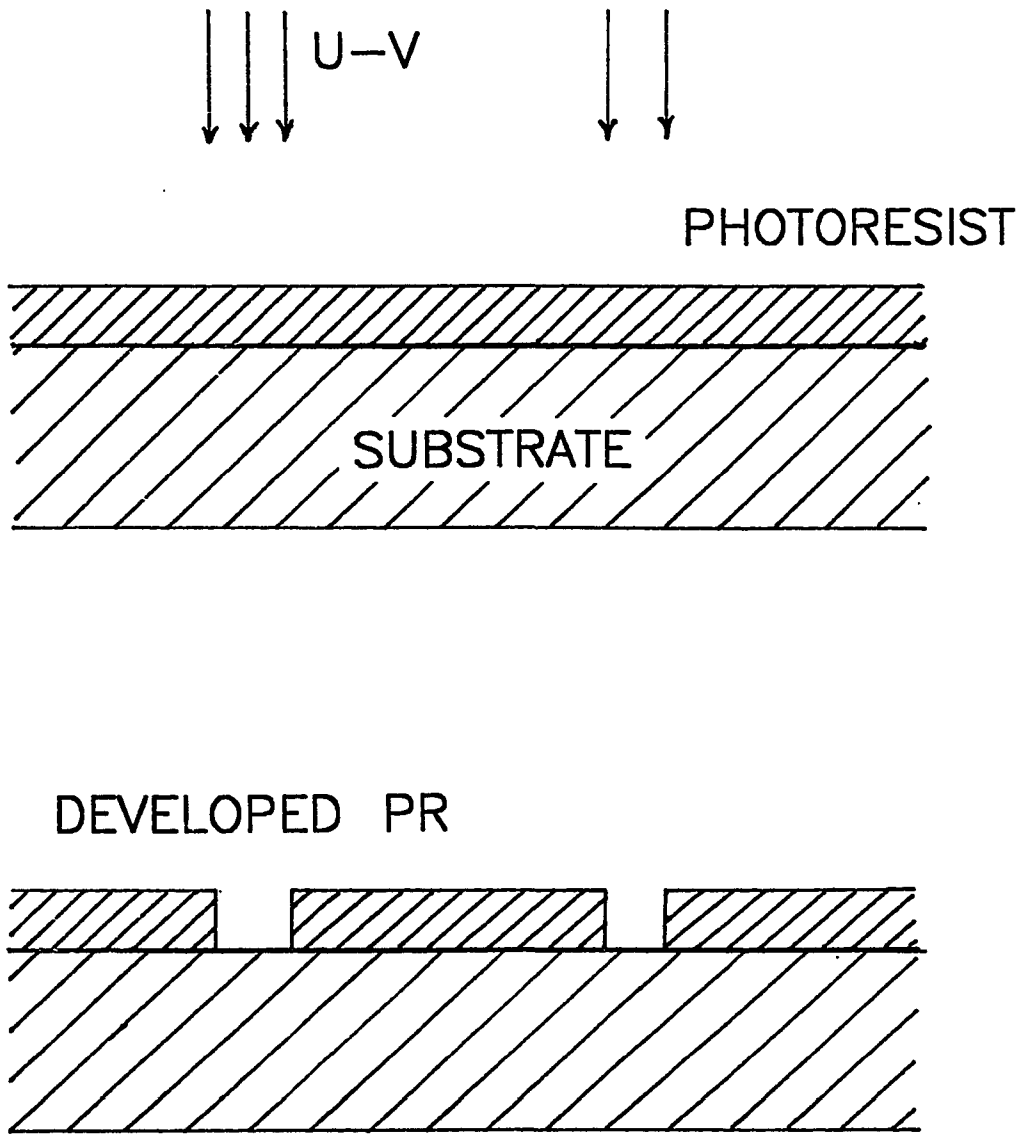

Figure 4.1 - Exposure and development of photoresist.

being developed. Instead the unexposed areas are removed by the developer solution.

4.2 Optical Lithography

Although there are many resists used for optical lithography, we fabricated using two common types: AZ-1350J and AZ-4110. Both are exposed with U-V and in general their characteristics are quite similar. A substantial amount of literature exists from the manufacturers regarding their characteristics. This section will briefly outline some of them.

The resists are usually spun at 4000-6000 rpm for a time period of 30 seconds to 1 minute. This is followed by baking at a temperature of either 70 °C or 90 °C for 20 minutes. The thickness of the resulting coating is dependent on the spin speed and time, and the solvent content of the resist, with nominal coatings being about 1 μm.

Better results are obtained when the bake is performed at 90 °C. The resist will have better resolution when patterned and will also be more resilient to latter chemical processing. However, if soft metals (such as Pb or Sn) already exist on the substrate, then high temperature bakes must be avoided. Most soft metals have a tendency to form hillocks when baked at 90 °C.

Both resists exhibit good sensitivity to U-V at a wavelength of approximately 320 nm. Depending on the resist thickness, exposure times may range from 30 to 90 seconds, usually at an intensity of 11 mW/cm^2. Afterwards, the substrate is soaked in a developer

solution. The developer is a base consisting of a solution of NaOH or KOH diluted with deionized water. This solution attacks the whole resist, but removes the U-V exposed areas at a much faster rate. Once this exposed resist has been completely removed, the substrate is again rinsed in deionized water to completely remove the developer and blown dry with clean N_2 gas.

The resolution (smallest feature) that can be patterned with optical lithography without too much effort is about 1 μm. This limit is due to diffraction effects from the edge of the mask pattern and the thickness of the resist. It is possible to improve on this resolution (down to about 0.4 μm) using thinned resists and ensuring good contact between the substrate and the mask. However, the process can then become rather laborious. In such cases, it is the easier to use electron beam lithography.

4.3 Electron Beam Lithography

Besides flexibility, the other main advantage of electron beam lithography is the resolution that can be obtained. However, it is more of a time consuming process. The resists are based on methyl-merthacrylates (PMMA or MMA) and must be baked at very high temperatures (220 °C) for about 30 minutes. This high-temperature bake often precludes using the resist on substrates that already contain thin-film patterns of "soft" metals.

The resist is patterned using a computer-controlled electron beam. The beam is typically 100 Å in diameter so that in principle it is possible to form patterns on this size scale. However in practice,

the resolution is limited by backscattering from the substrate and depends on the electron beam's flux and voltage. Ways to circumvent this problem are described in the next section.

4.4 Lift-off

Lift-off refers to the process by which the resist stencil is dissolved following thin film deposition. A common problem in this process arises from the tendency of a film to adhere to the walls of the photoresist pattern and hence be continuous (Figure 4.2). Consequently, during lift-off the film tears at the outline of the pattern, causing a ragged edge. This is specially true for sputtered films where the deposition is not directional. The ragged edges can cause step coverage problems or microshorts during subsequent processing.

One way to alleviate this problem is to try to form a pattern where there is an overhang in the resist profile (Figure 4.3). Then there will be a natural break in the film during the deposition. The overhang can be formed by a chlorobenzene soak of the photoresist after the exposure step [41]. The soak hardens the top layers of the resist, causing it to develop more slowly and forming an overhang when the developing is completed.

There are numerous drawbacks to the chlorobenzene soak procedure. It is an extremely unreliable process that is sensitive to factors such as the ambient cleanroom temperature and humidity, or the bath temperatures of the chlorobenzene and the developer. The process will also only work on AZ-1350J and even for this resist, the

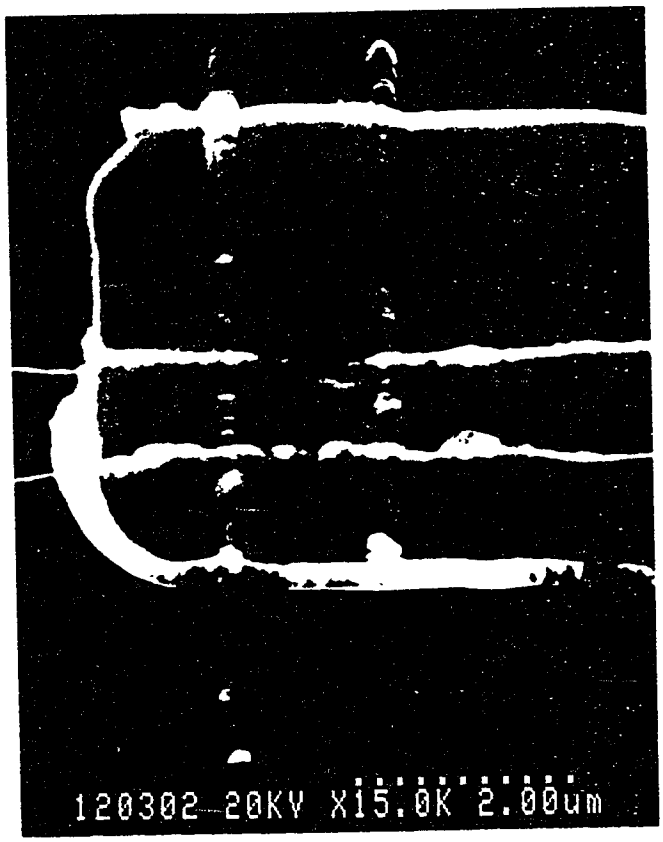

Figure 4.2 - Tears at film edges due to poor liftoff.

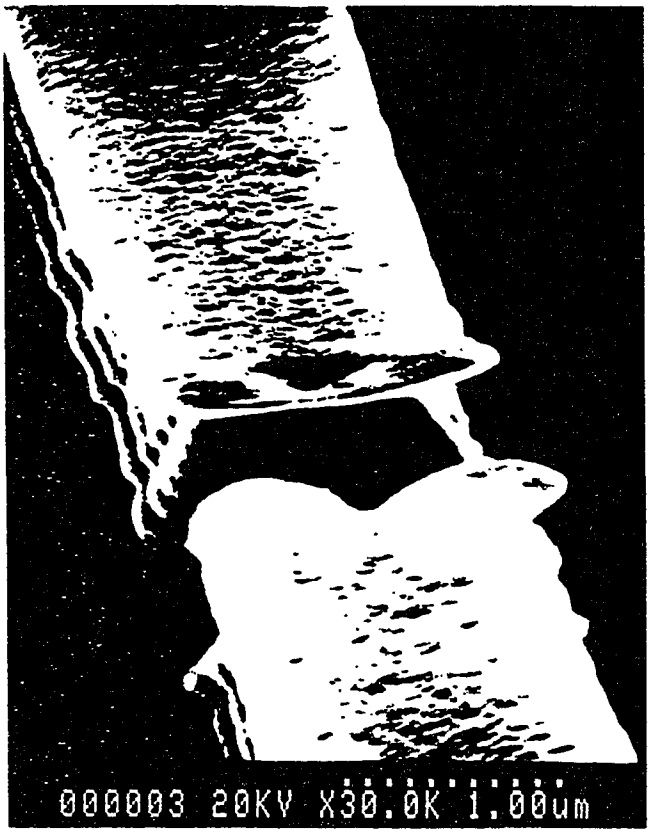

Figure 4.3 - Photoresist overhang formed by a chlorobenzene soak.

processing parameters will vary for different resist bottles. In particular, during the late summer months in our cleanroom, an 8 minute soak in chlorobenzene at a temperature of 27 °C followed by developing in AZ-351 developer diluted 5-1 with water, yields an overhang of approximately 0.2 μm.

There is another procedure developed by Dolan [42] for constructing overhangs that is much more reliable, although slightly more time consuming (Figure 4.4). It involves laying down two resist layers separated by a thin metallic layer. The lower resist layer is spun and baked and the entire substrate is massively over-exposed without a mask. Then a thin film is deposited on this exposed resist and finally a second layer of resist is spun and baked. The role of the intermediate metallic film is to prevent the lower resist from dissolving when the top resist is spun. The top resist layer in then patterned in the usual fashion (without a chlorobenzene soak). The metallic layer is then etched away, either through a wet chemical etch or by a plasma etch. Finally, the exposed area of the lower resist layer is developed in a weak developer solution. Since this lower layer is blanket-exposed, it will develop away easily and will form an undercut of a few microns beneath the top pattern. The size of the undercut can be easily controlled by the developing time.

The process is very forgiving and reproducible and can be used on almost any type of resist. For our cleanroom, the following parameters were used for AZ-1350J. The first layer was spun at 6500 rpm for 40 seconds, baked at 70 °C for 20 minutes, and exposed for 1.5 minutes at a U-V intensity of 11 mW/cm^2. The intermediate

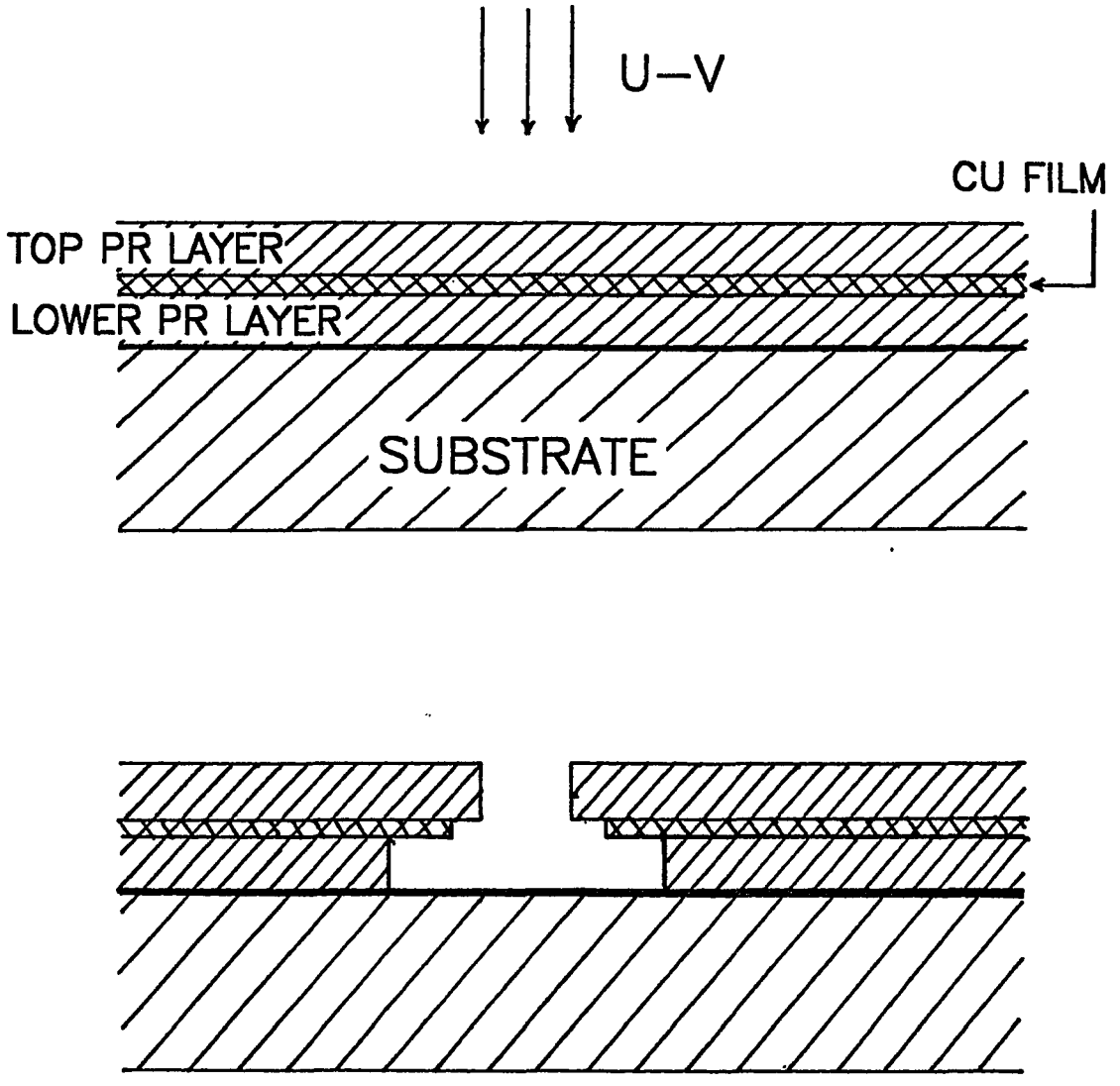

Figure 4.4 - Two-layer photoresist process used for constructing overhangs and shadow evaporation techniques.

metallic layer consisted of 400 Å of Cu. The top resist layer was spun and baked under identical conditions as the lower layer. After the pattern was formed on the top layer, the Cu was etched away in a solution of 30 mg of $FeCl_3$ in a liter of water in a time of 20 seconds. The lower layer was then developed in AZ-351 developer diluted 5 parts to 1 with water for 10-15 seconds. This process typically yielded undercuts around 5 μm.

One minor difficulty with this technique is possible reticulation of the lower resist layer. When reticulation occurs, the lower resist is no longer smooth and can become rather rough, resembling the surface of an orange peel. The effect is caused when an over-exposed resist is baked at high temperatures. Performing the bakes at 70 °C helps minimize this problem.

This technique can also be used for electron beam resists. In electron beam patterning, it is not necessary to blanket-expose the lower layer. The beam also easily penetrates the thin metallic layer between the two resists. In this process, a lower resist is chosen that is more sensitive to the electron beam. When the beam backscatters from the substrate surface, it spreads and is absorbed in the lower resist layer. This causes an overhang to naturally form during the development.

The bi-layer resist method is an elegant technique that has other applications. For example it can be used to make ultra-small-area devices through a shadow evaporation technique [42]. The extra processing time is well worth the effort in the long run through gains in the processing yield and reproducibility. It is also a

necessity for sputtered films since these films are not deposited directionally and will deposit on resist walls unless the overhang is extreme.

4.5 Metallurgy

A Josephson junction consists of two superconductors separated by a thin insulating barrier. The thickness of the barrier in a typical junction is about 20 to 30 Å. In order for the device to be of high quality, this barrier must be continuous and free of pinholes. It must also be robust enough to be able to withstand thermal cycling and should not deteriorate with time.

There are two classes of superconducting materials used for fabricating Josephson devices: "soft" metals such as Pb or Sn and refractory metals such as Nb, V, or Ta. Although Pb based device are easy to fabricate, they are not robust and lack reproducibility in their characteristics. On the other hand, fabricating refractory metal devices is more complicated. However they are very robust and are able to withstand thermal cycling exceedingly well.

4.6 Pb-based Devices

In a simple Josephson device fabricated out of Pb, a narrow strip of the superconductor is first deposited through a photoresist stencil. After lift-off, another strip is patterned orthogonal to the existing strip (Figure 4.5). The overlapping area is cleaned by ion milling with Ar followed by growing a thin insulating oxide on the film. Finally the top electrode is patterned and deposited.

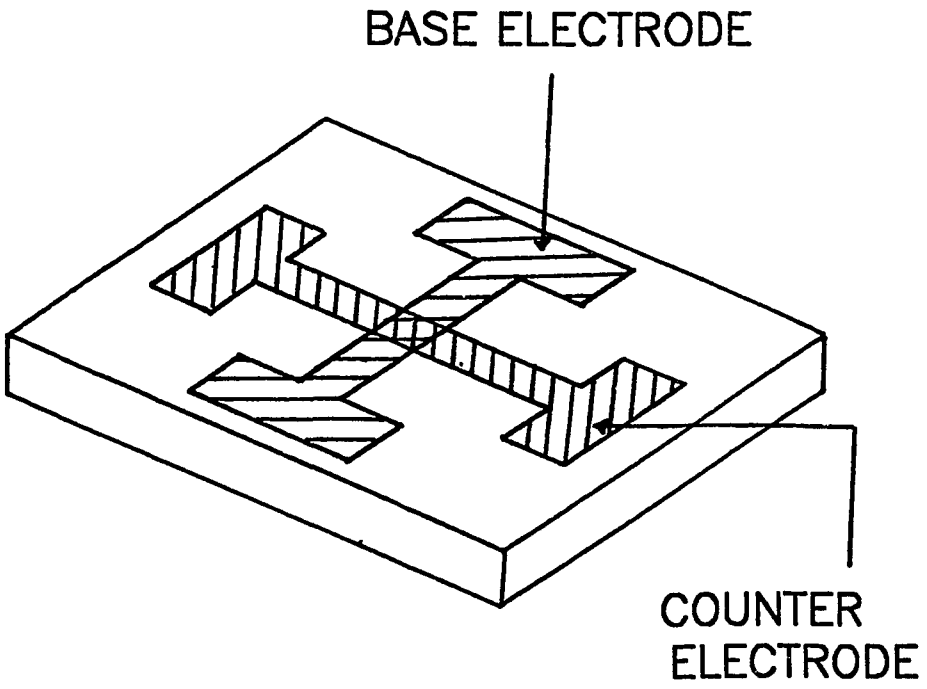

Figure 4.5 - Diagram of a simple overlap type Josephson junction.

The major disadvantage of Pb-based devices is the poor quality of Pb films. Evaporated Pb films have an FCC crystal structure which in thin films is mechanically unstable [43]. It has a tendency to clump and form hillocks, especially if the film undergoes thermal cycling, either during resist bakes or cryogenic cooling. The film is also not rugged and will scratch off easily during handling.

Extensive work was done at IBM in order to improve the quality of Pb films through alloying [44,45]. Numerous alloys were used in order to improve the mechanical stability and surface smoothness of the films. In 1981, Lahiri [43] developed an alloy of Au (2%) + Pb + In (10%) (by weight). In this process, the Pb grain boundaries are filled by a Au-In_2 alloy. The excess In also migrated to the surface, forming a protective layer of In_2O_3. The counter-electrode consisted of Pb-Bi or Pb-Au(2%). However by using an alloy, the transition temperature (and the gap energy) will be reduced, especially by a high In content.

In such devices, the insulating barrier is formed by first stripping the film surface of any oxides or impurities that have formed during the processing steps. The cleaning is formed by exposing the film to an Ar ion beam of low energy (300 eV) at a flux of 0.4 mA/cm^2 for about 30 sec. The beam originates from a Kauffman-type ion source [46].

After cleaning, a controlled oxide is grown, either thermally by allowing a few hundred milli-Torrs of O_2 into the chamber or by initiating a oxygen plasma (dc or rf) in the chamber. In both cases, the critical current density of the device is dependent on the

oxidation time and pressure. Finally, the counter-electrode is deposited, completing the S-I-S structure and forming the junction.

There are many factors that control the characteristics of Pb devices and contribute to their irreproducibility. For example, since alloys are used for the base electrode, the oxidation process will not only form various oxides of Pb, but also In_2O_3. In_2O_3 forms a Schottky barrier instead of a regular tunnel barrier and the two barriers have drastically different characteristics. It is desirable to form only In_2O_3 in the junction barrier since it is more rugged and its oxidation parameters are more reproducible. However, most of our junctions had barriers that consisted of both oxides. Since the grain size in the film can be on the order of the junction size, critical currents can vary greatly depending on the oxide material in the device.

Another problem that arose in our fabrication was the suppression of the Josephson current when the oxidation was performed in a pure oxygen plasma. Although we have no definite proof as to the cause of the problem, we feel it is either due to pure O_2 trapped in the barrier (which is magnetic) or by a normal layer of metal next to the barrier. The problem can be alleviated by using an Ar(10%) $+O_2$ mixture for the oxidation plasma. Coating the discharge electrode with either Pb or In can also greatly affect the critical current density, J_c, because of secondary sputtering off the electrode.

We fabricated devices with J_c's in the 10^3 - 10^4 A/cm^2 range. A typical Pb I-V is shown in figure 4.6. In this device, the base electrode consisted of a sequential evaporation of Au (2%) + Pb +

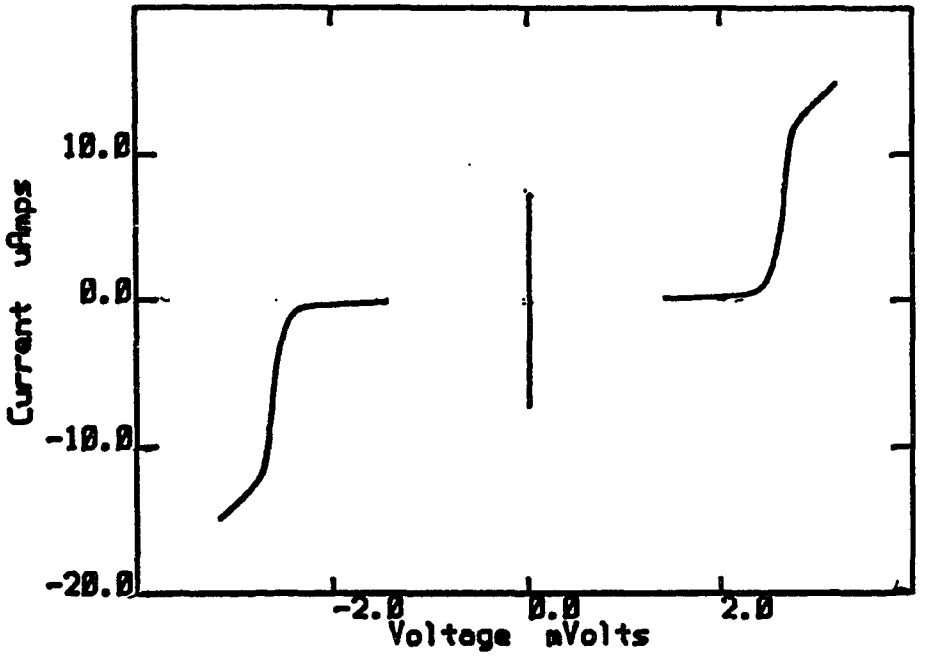

Figure 4.6 - I-V characteristics of a 1 μm^2 Pb device at 4.2 K.

In (10%). Ion mill cleaning was done at a flux of 0.4 mA/cm^2 at 300 V for 30 seconds and the oxide barrier was formed using a dc glow discharge in a mixture of Ar (10%) + O_2 at a pressure of 100 mTorrs for 15 minutes. The counter electrode consisted of Pb - AU (2%) alloy.

These devices were more rugged than pure Pb devices and able to withstand pure 2 to 3 thermal cyclings before becoming shorts. However, with each cycling, the quality of the device deteriorated. It should be noted that research groups at IBM were able to fabricate devices that were more rugged [44]. Although our junction were equal or better in quality, we were never able to fabricate devices that had very good stability. In summary, although theses devices are easy to fabricate, they are not robust nor very reproducible. The author's perseverance was tested on numerous occasions by Pb devices that had gone bad because of thermal cycling.

4.7 Refractory Metal Devices

Devices fabricated from refractory metals such as Nb pose different challenges than Pb-based devices. Although they are more difficult to fabricate, there is a fair amount of reproducibility in the successful devices. The junctions are also much more rugged and their characteristics will not change with time or thermal cycling.

A major consideration in fabricating Nb films is the cleanliness of the deposition system. This is not a problem for Pb devices since the superconducting properties of Pb are not affected by non-magnetic impurities. However Nb has a tendency to getter oxygen and is

extremely sensitive to other impurities. For example, hydrocarbons will cause the formation of NbC, which is a semiconductor. For this reason, it is imperative to have a system dedicated solely to Nb. Our best Nb films and devices are obtained from a cryo-pumped deposition system where only Nb and Al are deposited. The base pressure of the system is in the high 10^{-9} to low 10^{-8} torr range. The major advantage of a cryopump is that the pumping speed does not have to be throttled down when the sputtering gas is allowed into the chamber. High deposition rates (> 20 Å/sec) also yield better quality films.

During the early years of Nb fabrication, the process used was similar to Pb technology. The insulating barrier was formed after suitable cleaning by using native oxide techniques [47]. The main difficulty is that Nb forms numerous oxides, some of which are metallic, semiconducting, or even superconducting. The problem is exasperated by the fact that the desired oxide, Nb_2O_5, has the lowest rate of formation of all the Nb oxides.

The usual technique for forming Nb_2O_5 barriers is by rf plasma oxidation. Immediately after ion-mill cleaning, an rf plasma of pure oxygen is initiated in the chamber for a few minutes. Since the oxidation process is highly energetic, the resulting oxide will consist mainly of Nb_2O_5. Afterwards, the counter electrode is deposited, completing the S-I-S sandwich. The counter electrode cannot be made of Nb since it has a tendency to absorb oxygen from the insulating barrier and degrade it. Usually a Pb alloy is used instead.

There is another oxidation technique developed by Kleinsasser [48]. In this method, the oxidation is done by using a Kaufmann type ion mill. The gas used is a combination of Ar and O_2. High-energy (a few hundred eV) oxygen ions are impinged on the film, forming Nb_2O_5.

We have made Nb-Pb junctions using both of the above techniques. However, the yields were low and the junction quality was rather poor and not comparable to our Pb devices. This fact seems to be common with other groups fabricating these devices also. The device quality seems to be extremely dependent on the particular deposition system.

The major breakthrough in Nb fabrication technology occurred in 1981 when Kroger [49] developed the Selective Niobium Anodization Process (SNAP) (Figure 4.7). In this technique, a layer of Nb is deposited on the whole wafer. This is immediately followed by depositing a thin Al layer without breaking vacuum. The Al layer is then thermally oxidized. Finally the Nb counter electrode is deposited. In this manner, a sandwich of Nb-Al/Al_2O_3-Nb is formed over the whole substrate. The junction area is formed by selective anodization of parts of the top electrode. Subsequently the technique was improved upon by Gurvitch [50] who, in place of anodization, plasma-etched away parts of the counter electrode. The etching technique is convenient because Al_2O_3 acts as an effective etch stop, preventing the base electrode from being removed. After etching, the exposed area was either anodized or covered with an insulator.

The success of this technique mainly depends on the wetting

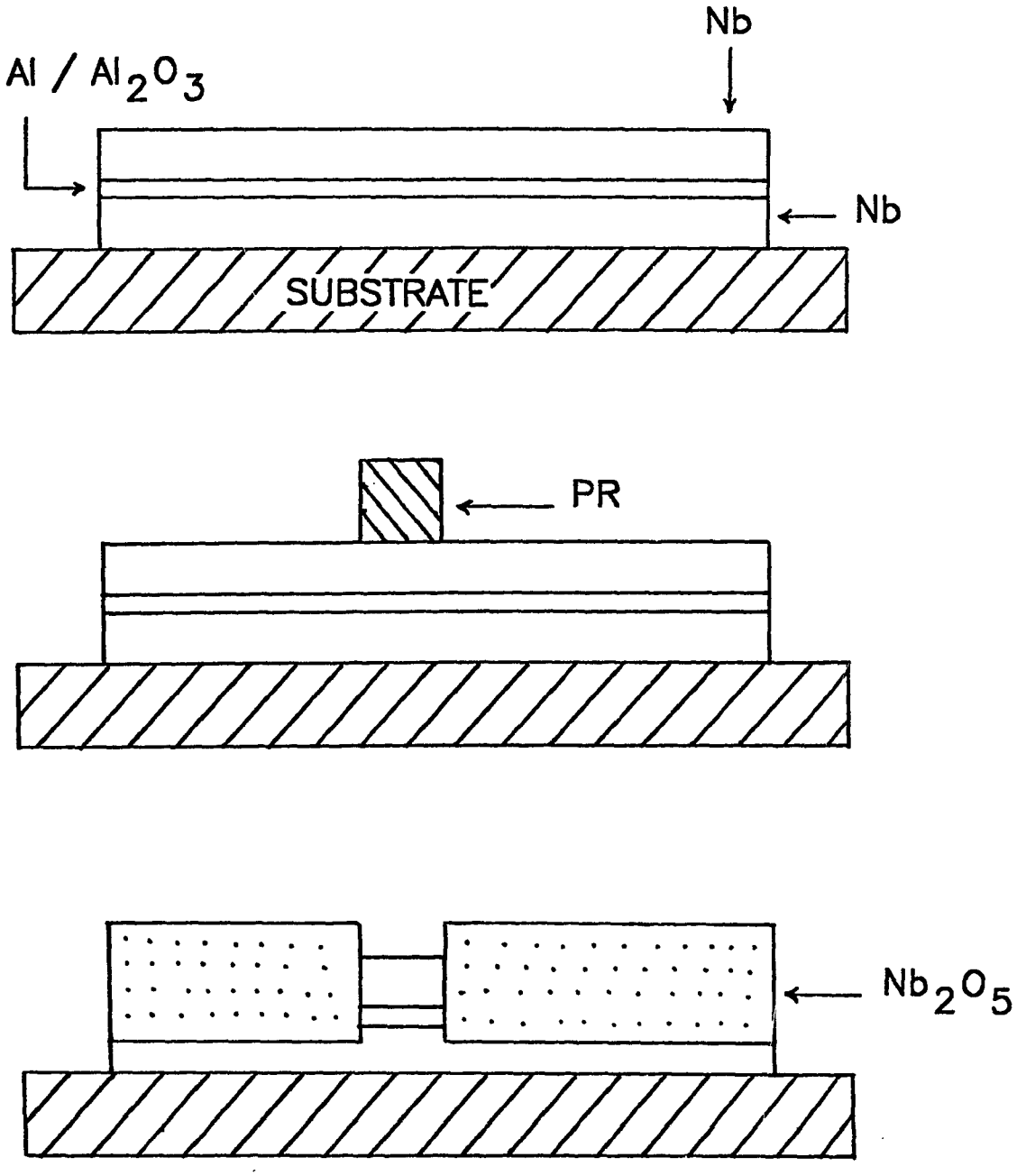

Figure 4.7 - Diagram of the SNAP process.

properties of Al on refractory metals. It has been reported that Al films as thin as 10 Å can uniformly cover a fresh Nb surface [51]. Al is also easily oxidized and forms a tough insulating barrier that does not easily deteriorate. Although the junction quality is excellent, small area junctions could not be made with this technique. The lower limit for junction size was about 100 μm^2.

This problem existed until its cause was independently determined by work at Fujitsu [52], NTT [53], and also our laboratory [54]. Its underlying cause is the intrinsic stress present in sputtered Nb films [55]. The stress can be either compressive or tensile and is largely dependent upon the sputtering pressure and to a smaller extent, the deposition rate. As large areas of the top electrode are removed, there is a tendency for the lower Nb film to buckle, causing a break and consequently leakage in the insulating barrier.

One solution is to try to deposit the trilayer at a pressure that results in zero stress in the film. Although it is possible to fabricate small junctions in this manner, the procedure is rather tricky since the stress is extremely sensitive to the sputtering pressure. A more elegant solution is to deposit a small trilayer area through a photoresist lift-off stencil. In this manner, the area of counter electrode removed is small and the whole issue of film stress is avoided.

Using slight modifications of the above technique, we have made the highest quality, small area (< 1 μm2) all-Nb junctions reported to date. In our procedure, we deposit a trilayer of Nb-Al/Al_2O_3-Nb sandwich on a quartz substrate (Figures 4.8, 4.9). The deposition

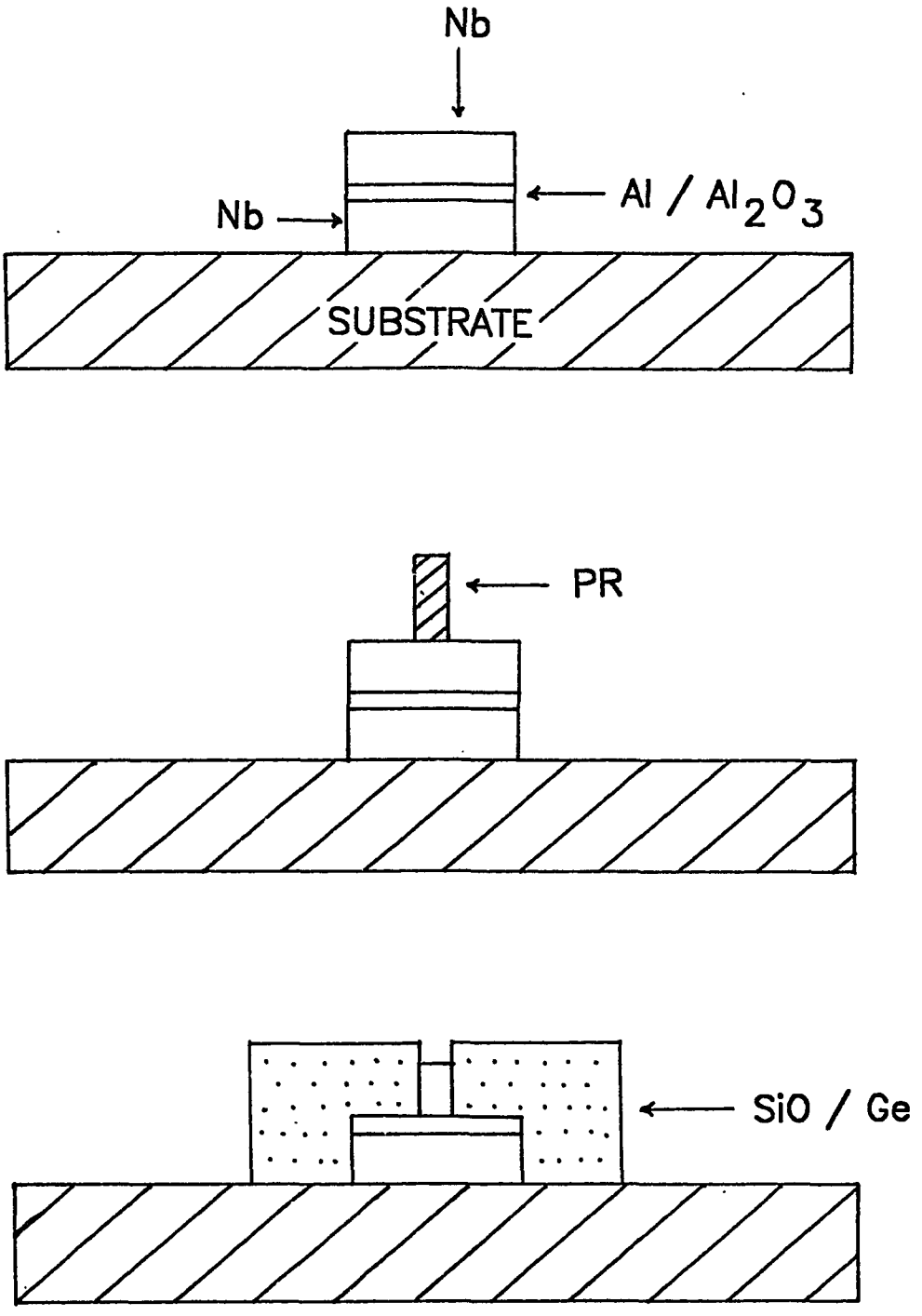

Figure 4.8 - Diagram of our modified SNEP fabrication process.

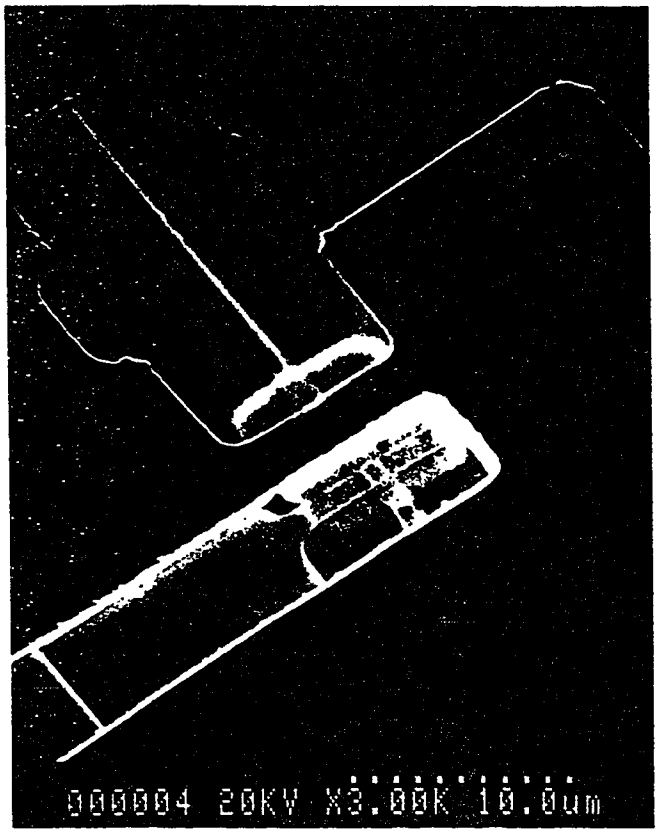

Figure 4.9 - Electron micrograph of a sub-micron Nb device.

is done through a two-layer resist stencil to obtain clean lift-off. The base Nb layer is deposited at a rate of 30 Å/s and its thickness is about 1000 Å. The substrate is then cooled to 77 K and a 40 Å layer of Al is deposited. (Al layers thicker than 50 Å tend to result in lower quality junctions and will cause a suppression of the Josephson supercurrent). The cooling is done to prevent the Al from clumping on the Nb surface and to prevent the formation of Nb-Al alloys. After the Al deposition, a few hundred milli-Torrs of pure O_2 is allowed into the chamber for 20 to 30 minutes to oxidize the Al and obtain the desired current density. Following the oxidation, the chamber is then pumped for a minimum of 5 hours and the top Nb layer (1000 Å) is then deposited.

Once the trilayer is formed, the junction area is defined in a two-step process. First a 1 μm line of photoresist is patterned on the trilayer. The top Nb layer is then removed on either side of this line in a reactive ion etcher. The etching gas used is CF_4 and the etcher is operated at a pressure of 40 mTorrs and a power density of 0.05 W/cm^2. Typical etching rates are about 200 Å/min for Nb. A thin layer of Al_2O_3 acts as an effective etch stop as long as it has not been exposed to air, and therefore over-etching is not possible during the first etch step. Immediately after etching, the sample is moved into an evaporation system where 2000 Å of insulator (usually a SiO/Ge alloy) are deposited. The etching and deposition process is again repeated on a photoresist line patterned orthogonally to the first line. As a result, a 1 μm2 square Nb device is left on the substrate. At this point connecting lines are patterned for the base

and counter electrodes. The main advantage of forming the junction area in two steps is that it facilitates the lithography drastically for small-area junctions.

We have made devices using this technique that are robust and exhibit excellent I-V characteristics (Figure 4.10). Typical values for sub-gap (@ 2mV) to normal-state resistance ratios are about 35 at 4.2 K and as high as 60 at 1 K. The previously best-reported values were about 20 for all-Nb junctions [53]. There is also considerable reproducibilty in this technique. Devices made on one substrate are identical and devices on different substrates fabricated in the same manner are also nearly alike. In general, Nb fabrication has greatly reduced the amount of time and effort needed for fabrication of Josephson devices. Their excellent characteristics, reproducibilty, and ability to withstand thermal cycling have made experiments much more successful.

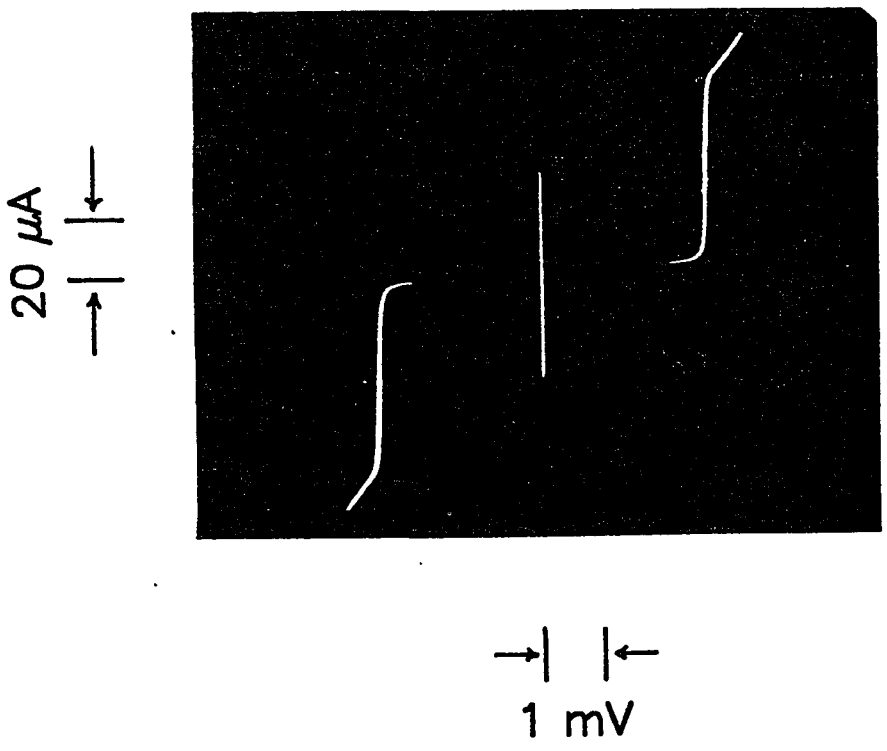

Figure 4.10 - I-V characteristics of a 1 μm^2 Nb device.

Chapter 5

DATA AND ANALYSIS

Our efforts have been concentrated on two issues in this field. We have tried to shed light on the dissipation question by performing an experiment in which we could vary in-situ the resistance of a single junction. By so doing, we hoped to determine what exactly is the resistance that is relevant in the L-C model and whether it exhibits any frequency dependent behavior.

We were also interested in searching for MQT in multi-dimensional potentials. We have been able to observe MQT in the two-dimensional potential of a dc SQUID. We also see some interesting effects on the classical thermal activation escape rate, possibly due to the interaction of the two modes in the potential. This chapter will elucidate our results and propose possible models for some of the effects we observe.

5.1 Measurement Techniques

As was previously mentioned, the signature for the escape of the particle from the metastable wells is the jump to the dc voltage state. In principal, one could bias the current at a level below the critical current of the device and measure the time it takes for the jump to the finite voltage state to occur. By obtaining a distribution of such events, a mean lifetime could be established. However, most measurements are done in an easier, if more indirect fashion. Usually, the bias current is increased at a known rate

until a voltage appears, and the bias current at which this jump occurs is then recorded. Increasing the bias will cause the potential barrier to be lowered. The switching current is a measure of the barrier height at which the escape occurs. If the intrinsic escape rate is high, then the jump can occur at a barrier height that is appreciable. As the temperature is lowered, the jump will occur at a lower barrier height, or larger bias current, until the quantum limit is reached.

The bias is ramped at low frequency, typically about 50 Hz, and a distribution P(I) of approximately 20,000 switching events is obtained at a fixed temperature. The distributions have a skewed Gaussian shape (Figure 5.1) and are characterized by their first and second moments, corresponding roughly to their peaks and widths. The skewness results from the increase in the escape rate as the bias is increased, causing the rate not to be constant across the distribution. Hence it is more likely for escape to occur at the higher bias currents.

These distributions can be deconvoluted to obtain actual rates [56]. P(I) is defined such that the probability of the junction switching to the finite voltage state in the current range I to I + ΔI is P(I)ΔI. To deconvolute the distribution, assume there is an ensemble of N junctions in the zero-voltage state at time t = 0. Then the number that have switched after a time t is

$$N\,P(I)dI = N(0)\,\Gamma dt \tag{5.1}$$

where Γ is the escape rate and N(0) is the number of junctions left in the unswitched state. Since

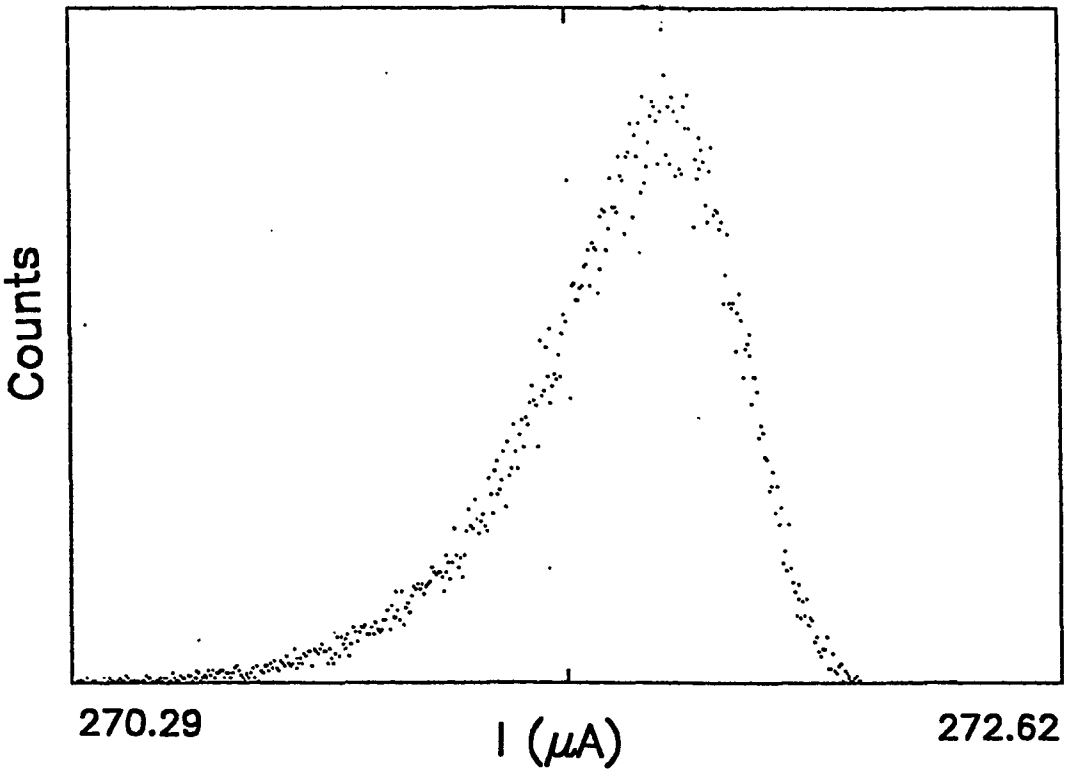

Figure 5.1 - Distribution of switching events as a function of bias current.

$$N(0) = N\left[1 - \int_0^I P(i)di\right] \tag{5.2}$$

we obtain the result

$$\Gamma(I) = \frac{P(I)\frac{dI}{dt}}{1 - \int_0^I P(i)di} . \tag{5.3}$$

In practice, we find it easier to use a theoretical prediction for the escape rate to simulate distribution peaks and widths and compare these to the experimentally derived results. Since the quantum escape rate is essentially independent of temperature, the signature for MQT would be the first and second moments not varying below a certain temperature.

There are numerous technical difficulties in trying to perform these experiments. The distribution widths are rather small and on the order of 0.1% of the thermodynamic critical current of the device with typical values of about 0.1 μA. The escape rate can also change by about an order of magnitude over a distribution width. Therefore a high degree of precision and accuracy is required in the electronic circuitry performing the measurements.

External noise sources can also wreak havoc on the measurements. Such noise sources, even at very low levels, can produce escape rates that are essentially temperature independent and which can be mistakenly identified as MQT. All leads to the device have to be carefully filtered to prevent external transients from causing noise induced escape. Since the plasma frequencies are typically about 100 GHz, the filters have to be effective in this frequency range. For these high frequencies, standard circuit elements such as inductors or capacitors do not behave as designed.

The noise isolation is achieved by two methods. There is some inductive isolation due to the length of the connecting leads. This is complemented by custom-designed inductors consisting of loosely coiled wire in a tube filled with copper powder. There are also conventional low pass filters designed to operate at lower frequencies in series with these high frequency filters.

Electromagnetic shielding is also of high concern. All measurements are done in an rf shielded room. The device is placed in a Cu can which is contained in a Meissner shield consisting of a bag made of Pb foil. Such shielding prevents stray magnetic fields from inducing fluctuations in the critical current of the device.

Temperature regulation is another area that requires special attention. All the measurements were done in a dilution refrigerator (Oxford model #600) which could achieve a base temperature of 10 mK. Since the switching distributions are sensitive to temperature changes in the thermal regime, stability must be maintained long enough to record a statistically significant number of switching events. Throughout the measurement process, a criterion was established in which temperature drifts of less than 10 mK in the time it took to record a distribution were deemed acceptable. It is also important to have good thermal contact between the thermometer and the sample by minimizing the Kapitza resistance. The sample was heat sunk using Apiezon N grease for the earlier measurements. The grease was later combined with Cu powder to improve the thermal contact.

The electronic circuitry is divided into two major sections

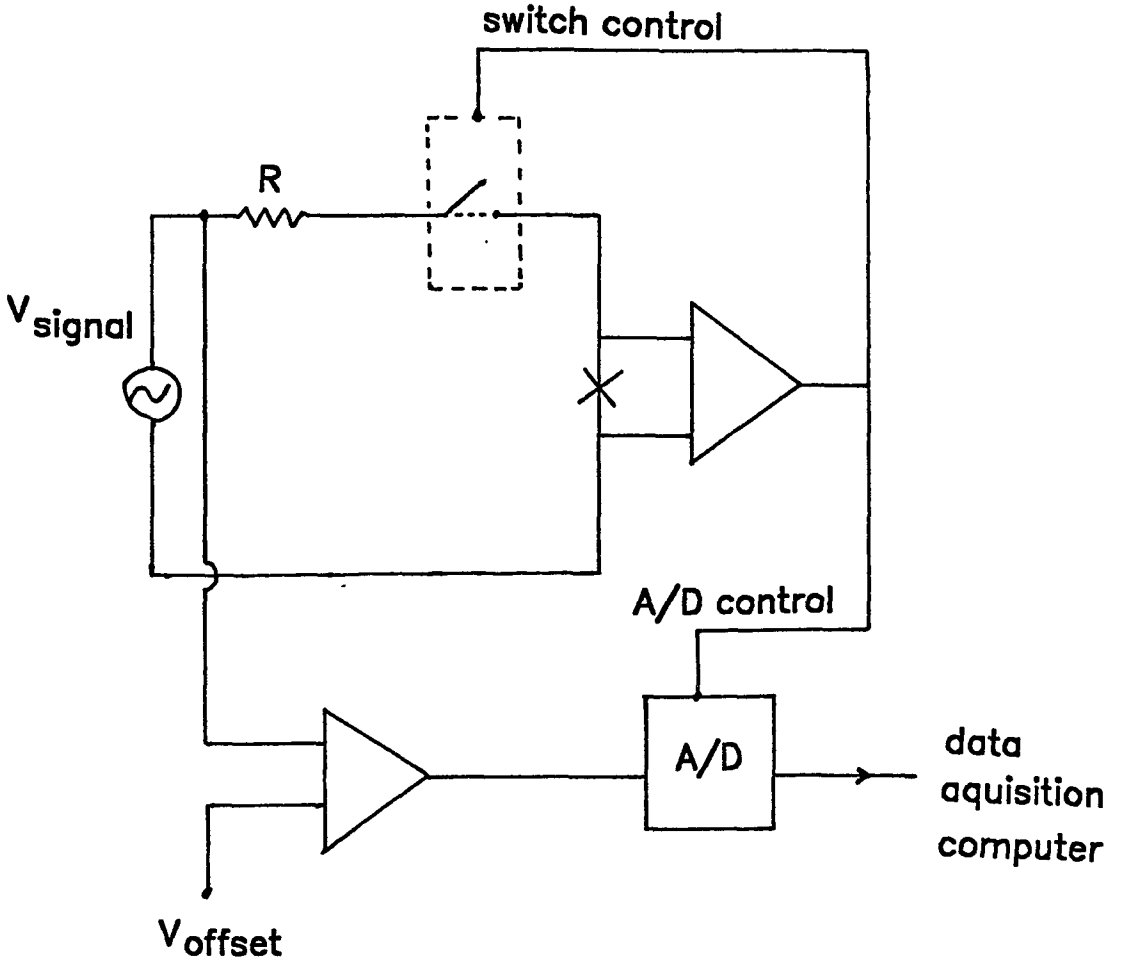

Figure 5.2 - Block diagram of the electronic circuitry used to obtain switching distributions.

(Figure 5.2). One part produces the current ramp used to drive the device and detect the voltage across the junction; the other monitors the ramp current using an A/D convertor and is computer-interfaced for data acquisition.

A major concern in designing a current ramp source is the cleanliness of the signal. If the low frequency signal used has spurious high frequency components, there is the possibility of noise-induced transitions. We used an HP function generator (model #3310B) which produced a voltage across a dropping resistor. The resistor acted to limit the current in the ramp circuit. The signal was sinusoidal and at a low frequency to ensure the integrity of the waveform through the filters. The signal was also routed through an FET switch that could be externally controlled. The voltage across the junction was monitored using an Ithaco preamplifier (model #1201).

Since the distribution widths are very narrow, it is necessary to enhance the resolution of our measurements before data acquisition takes place. This was accomplished by branching the signal ramp and feeding it differentially into the input of a second Ithaco preamplifier (model #1201). The other preamplifier input consisted of an offset voltage and the output was connected to the A/D convertor. The offset voltage was adjusted to ensure that the finite voltage transitions occured within the range of the A/D convertor. The width and resolution of the transitions was controlled by the gain of this second preamplifier. The convertor was triggered by the first preamplifier to take a measurement when a

dc voltage appeared across the junction. Both preamplifiers were set at full bandwidth to minimize measurement delays in the circuitry.

After the junction switches to the finite voltage state, power is dissipated in the device, producing local heating. In order to prevent this local heating of the junction, this trigger also opened the FET switch through which the signal to the device was routed after the current was read by the A/D. The switch did not reset until the beginning of the next ramp cycle. Calibration of the A/D bins can be calibrated into units of current was performed using the offset value, the path resistance, and the gain of the second preamplifier.

5.2 Data Analysis

A typical data set on a junction consists of measuring the peaks and widths of switching distributions at various temperatures. Once these distributions are obtained, they are compared to the predictions of the various theoretical models.

In order to perform these comparisons, it is necessary to know the value of device parameters such as the critical current, capacitance, and the damping resistance. In all cases, these values were derived initially from fits to the data in the thermal regime and whenever possible, compared to results obtained through independent methods. The difficulty with these fits is that they are much more sensitive to the parameters that appear in the exponent than the parameters that are in the prefactor of the rate expressions. Thus in the

thermal regime, these fits yield an accurate value for I_c and less precise values for R and C.

We tried to independently verify the value of as many of the parameters as possible to avoid relying strictly on fits. In the case of the junction capacitance, it is possible to obtain values to within a 20% accuracy from the geometry of the device and the dielectric constant of the insulator. For the resistance, the situation is not as clear. Since our devices did not have resistive thin film shunts, we had to obtain our resistance values from fits in the quantum regime. In this regime, the resistance appears in the exponent and the fit is very sensitive to its value.

There are also other methods that can be used to obtain the device parameters. For example, it is possible to measure the plasma frequency of the device directly by radiating the device with microwaves and looking for resonance enhancement of the escape rate at a specific microwave frequency [30]. We did not use this technique because we did not have a variable frequency microwave generator.

5.3 In-Situ Variation of the Resistance

We devised an experiment in which the resistance of a Josephson junction could be varied in-situ to clarify the nature of the dissipation. Our variable resistor consisted of a superconductor-insulator-normal metal (S-I-N) tunnel junction. Such a junction has a non-linear I-V characteristic and its dynamic resistance is dependent on the bias current (or voltage). The S-I-N junction was

coupled to the Josephson junction through capacitors whose values were much larger than the intrinsic capacitance of either junction (Figure 5.3).

The idea behind this configuration is that the resistance of the S-I-N junction can be externally controlled by a dc bias. The shunting capacitors will not allow the dc current to reach the Josephson junction. However the relevant oscillation frequencies important for escape out of the metastable wells are extremely high, and at these plasma frequencies, the shunting capacitors have a very low impedance and behave as shorts. Therefore the Josephson junction can "see" the S-I-N resistance without being affected by the dc bias used to set its value.

The Josephson junction was fabricated using Pb-alloy technology as outlined in chapter 4. Briefly, the base and counter electrodes consisted of Pb alloys and the oxide barrier was formed in an oxygen plasma generated by a dc glow discharge. The S-I-N device also was constructed in a similar fashion except for the counter-electrode, which was Cu. Each junction was approximately 1 μm^2 in area. The I-V characteristics of the devices are shown in figures 5.4 and 5.5. Figure 5.6 is a plot of the dynamic resistance of the S-I-N as a function of the bias voltage.

The shunting capacitors consisted of a trilayer sandwich of Pb-alloy, insulator, and Cu. The insulator was a layer of SiO 800Å thick, a layer of Ge 300Å thick, followed by another layer of SiO 800Å thick. The Ge prevented pinhole formation in the SiO. The area of the shunt capacitors was approximately 300 μm by 300 μm. The two

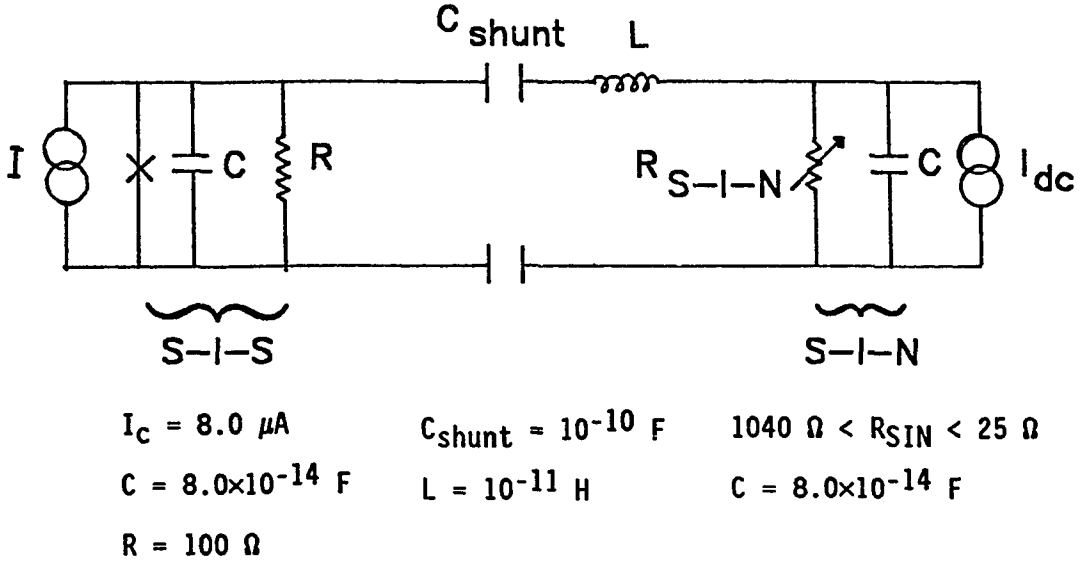

Figure 5.3 - Schematic diagram of a Josephson junction capacitively coupled to a S-I-N tunnel junction. The parameters of both devices are also listed.

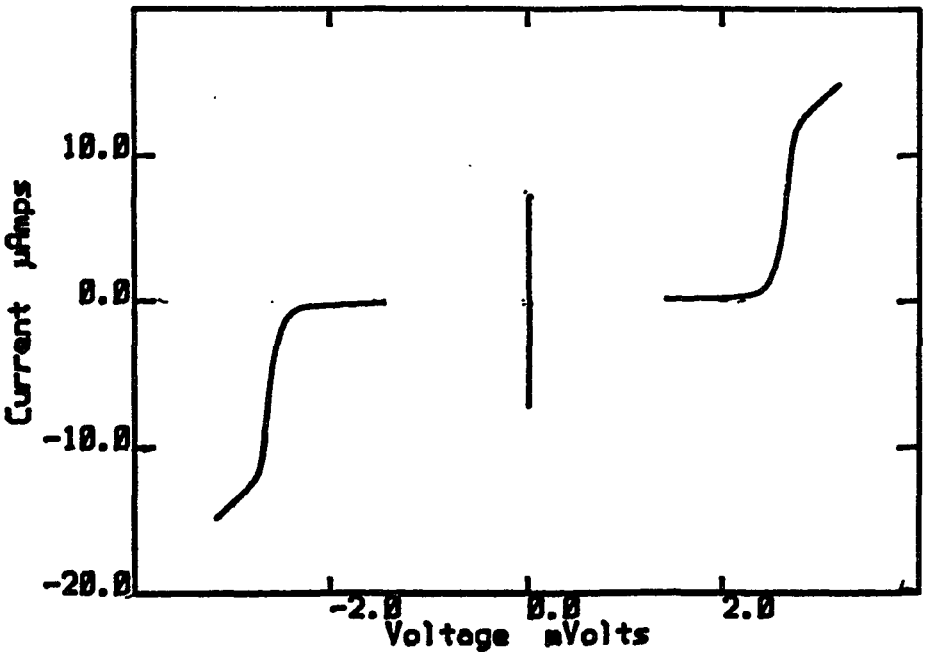

Figure 5.4 - I-V characteristics of the Pb-alloy device.

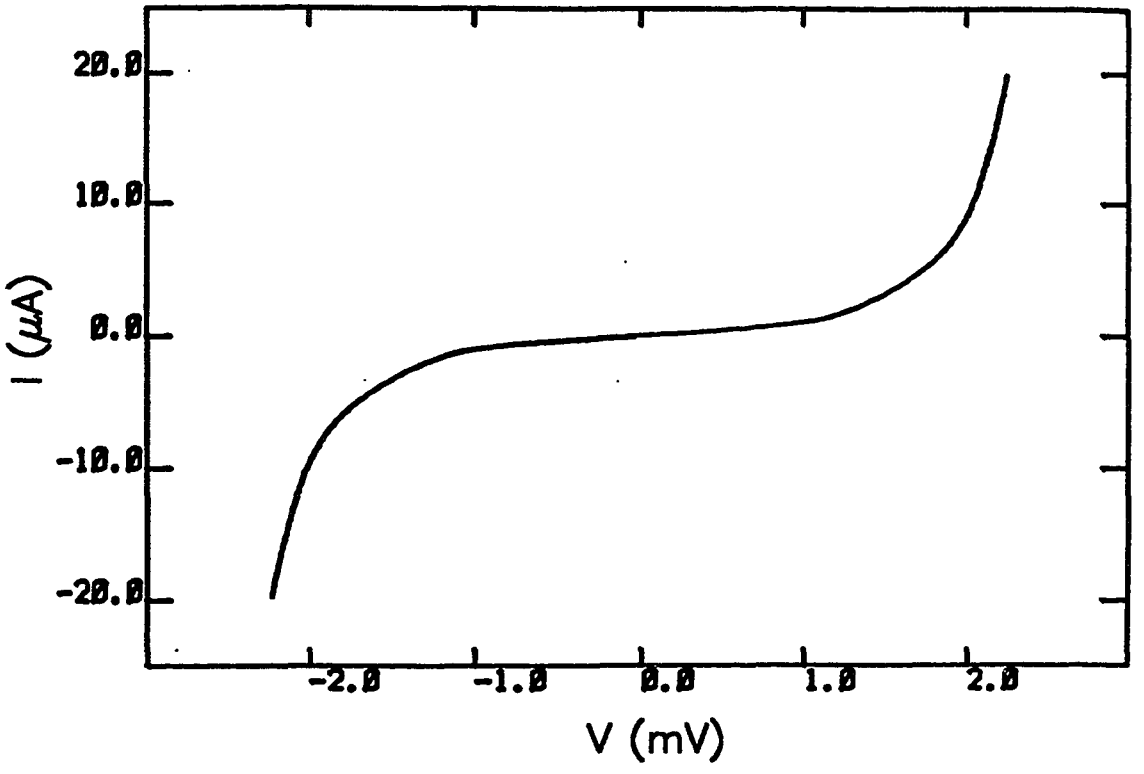

Figure 5.5 - I-V characteristics of the S-I-N device.

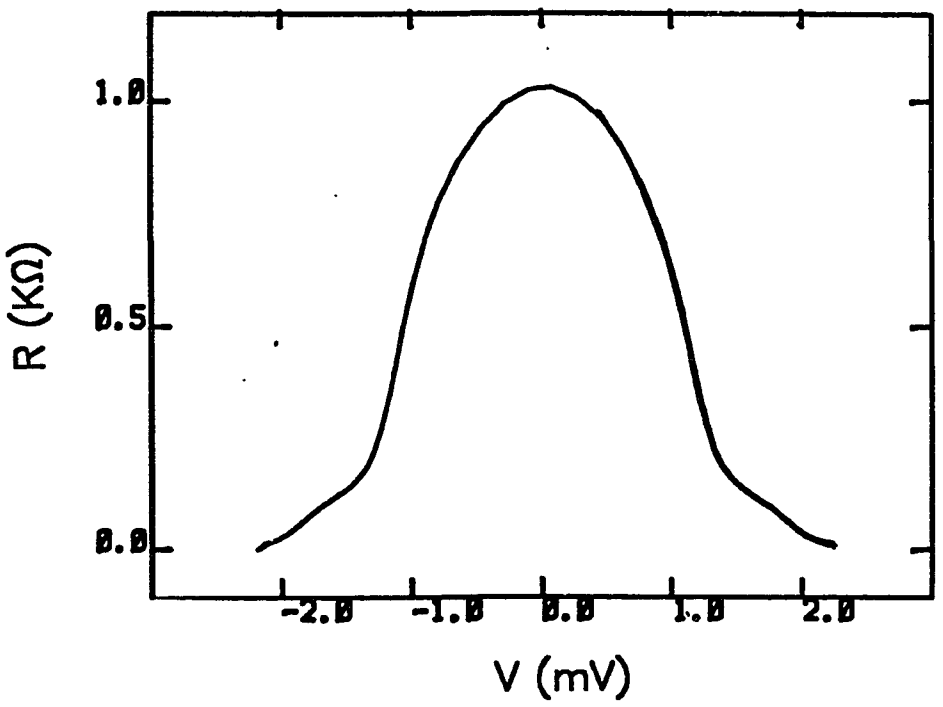

Figure 5.6 - Plot of dynamic resistance of the S-I-N device as a function of bias voltage.

devices were placed as close together as possible to reduce the impedance due to the loop inductance. The parameters for this device are given in figure 5.3.

Figure 5.7 shows the peak positions of the distributions vs. temperature with no bias on the S-I-N. As shown, the peaks of the distributions move to higher currents with decreasing temperature. At approximately 150 mK, the peaks flatten and become temperature independent, signifying MQT. From fits in the thermal regime, I_c and C are determined to be 8.0 μA and 80 fF respectively. The damping parameter is obtained by fitting the data in the quantum regime, yielding a value of R = 70 Ω . This value is very close to the normal state resistance of the device (100 Ω), in agreement with other work on unshunted junctions. It should be pointed out that since this resistance value is lower than the S-I-N resistance (at no bias), the dissipation at this point is determined by the intrinsic dissipation of the Josephson junction. The solid lines are theoretical fits to the data generated with the above parameters. The deviation from these fits near T_c is caused by enhancement of the escape rate due to quantum corrections from the thermal activation model.

An interesting effect occurs when a bias is applied to the S-I-N. Even at extremely low bias levels, the distributions begin to shift dramatically to lower currents. Figure 5.8 plots the shift in the distributions (with respect to no bias) as a function of the S-I-N bias at various temperatures. There is a noticeable bump in the shifts at the S-I-N gap voltage and the magnitude of this bump decays

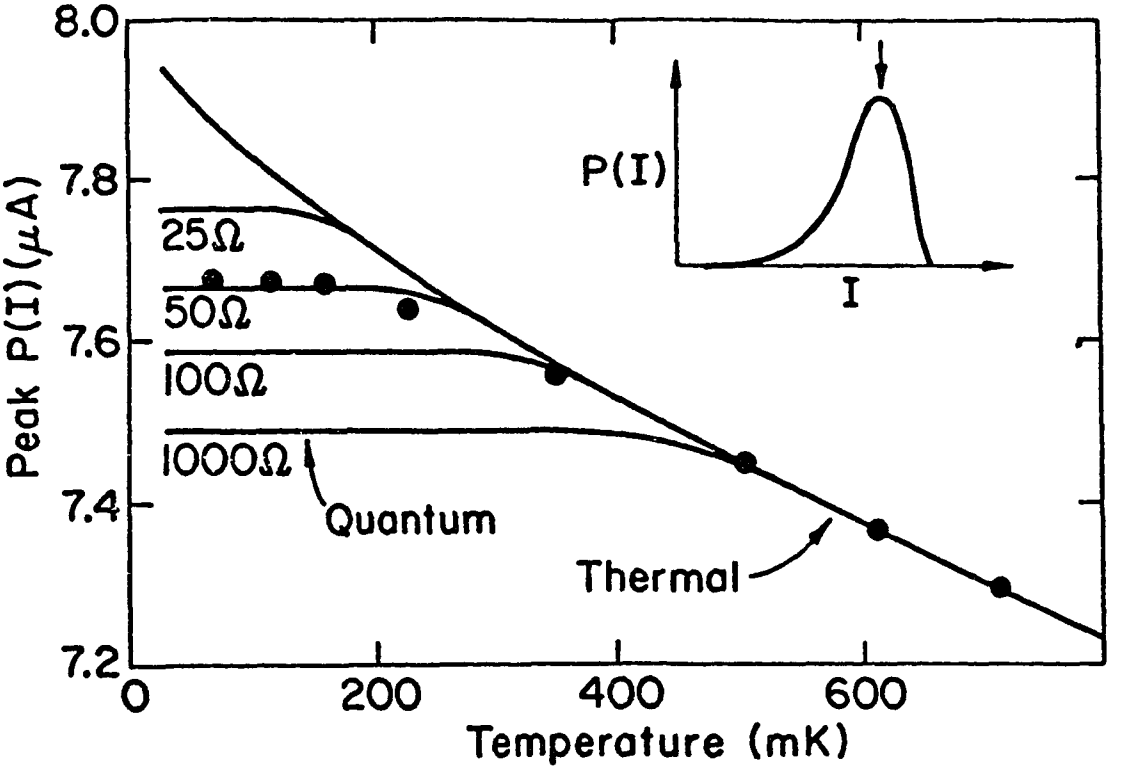

Figure 5.7 - Plot of the peaks of the switching distribution vs. temperature with no S-I-N bias. The peaks flatten at approximately 150 mK, signifying MQT.

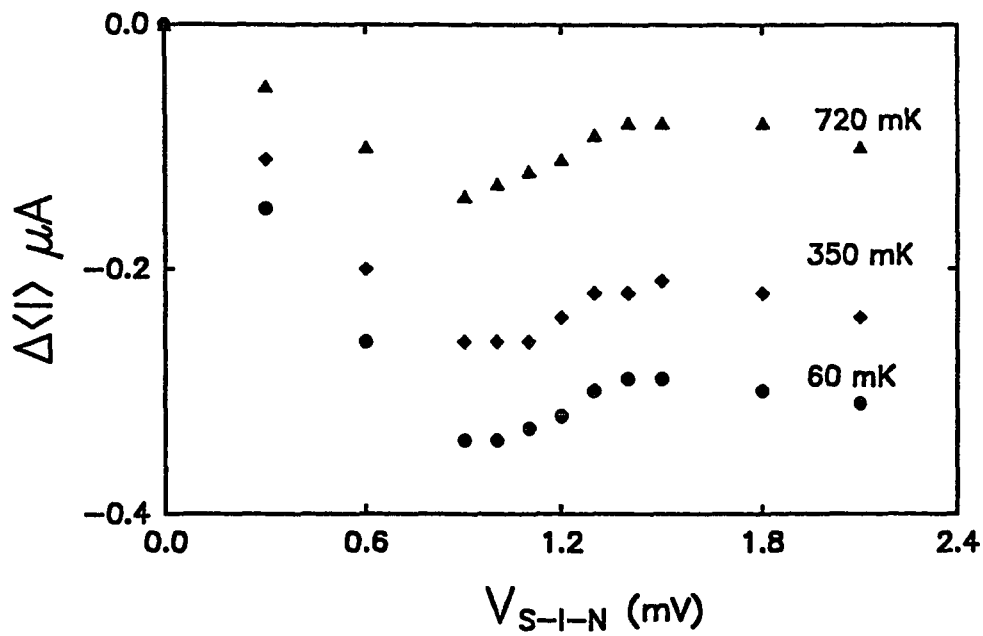

Figure 5.8 - Plot of the shift in the peaks of the switching distribution vs. S-I-N bias at various temperatures.

with increasing temperature. What is clear from the data is that unfortunately the effect is not due to a variation of the damping in the MQT regime. This observation is not based on the fact that the distributions move to lower currents instead of higher currents with increasing S-I-N bias, as predicted by the L-C model. If the effect was due to dissipation, it should become extremely small when the Josephson junction is in the thermal regime; it clearly does not.

We have tested various models to try to explain this data. Among them are magnetic field suppression of the Josephson current due to the S-I-N bias current, self-heating of the junction, and noise induced transitions caused by the S-I-N bias. After analysis, the first two possible causes can be ruled out while the third can be modelled to yield qualitative agreement with the data.

Magnetic flux effects can be ruled out by a few simple observations. First the shift in the peaks is not monotonically decreasing, as would be expected for the supercurrent suppression. In fact a worst case calculation for the amount of magnetic flux put through the Josephson junction by the S-I-N bias current yields a value on the order of $10^{-4}\ \Phi_0$, hardly a noticeable effect. Similar arguments can also be made for junction self-heating. Not only is the power dissipated in the S-I-N too low to be a factor, it is also monotonically increasing and would not be able to explain the bump in the data. Neither model can also explain the reduction of this effect with temperature.

A more likely scenario is that the effect is induced by shot noise through the S-I-N. This type of noise is the limiting case of

Johnson noise at very low temperatures. Its spectrum is white and it is characterized by a small number of electrons tunneling in bursts through the device. Such noise would cause escape from the metastable well of the Josephson junction by activation over the barrier.

The noise power spectrum in a S-I-N tuunel junction is given by [57]

$$P_n = \frac{eI_b}{2\pi}\left[(V + \hbar\omega/e)\coth\left(\frac{\hbar\omega + eV}{kT}\right) + (V - \hbar\omega/e)\coth\left(\frac{\hbar\omega - eV}{kT}\right)\right] \quad (5.3)$$

Here I_b is the tunnelling current through the S-I-N. For the temperature range of our measurements and for the plasma frequency of our Josephson junction, the above equation can be well approximated to yield an effective current noise,

$$I_n = \frac{I_b}{4\pi} . \quad (5.4)$$

Qualitatively, as the bias is increased, the dynamic resistance of the S-I-N decreases slowly at first and rapidly as the gap voltage is reached. When the S-I-N resistance is high, more of the current noise is routed to the Josephson device. As the S-I-N resistance becomes low, the noise current is shunted through this path, away from the Josephson junction. This shunting effect may explain the bump in the switching distributions at the S-I-N gap voltage. At this voltage, the noise current is minimized through the Josephson device.

Even though such a model is highly simplistic, it is able to qualitatively explain many other features of our data as well. As

the temperature is increased, thermal fluctuations become comparable to the noise-induced fluctuations, thereby diminishing the effect. A quantitative model has to treat possible reflections at the boundaries between the different materials as well.

Although this experiment is an exhaustive set of measurements on noise in S-I-N tunnel junctions, it did not answer many questions with regard to our original goal. One solution is to replace the S-I-N junction with some other form of non-linear resistor. One possibility we are presently studying is a thin film composed of amorphous In/In-Ox. By applying an electric field to this type of film, it is possible to modulate the carrier density and hence change the film resistance [58,59]. The main advantage this configuration is that no external current is passed through the variable resistor, thereby eliminating noise problems. This would also eliminate the need for the shunt capacitors. In designing such a circuit though, one must make certain that the capacitors used to apply the external electric field are small enough so as to not increase the effective junction capacitance dramatically.

5.4 MQT and Thermal Activation in DC SQUIDs

We have also extended our work in MQT to the two-dimensional potential of a dc SQUID [60,61]. Such a system is interesting because of various reasons. Since the potential is two-dimensional, there are two macroscopic degrees of freedom: the phase mode controlled by the bias current, and the flux mode caused by circulating currents induced by external flux. It is possible to

investigate the dynamics and interactions of these variables in various escape regimes.

In addition to the bias current, the external magnetic flux provides another degree of control for dc SQUID potentials. By varying the flux and the bias, both the depth and shape of the barrier can be modified. It is possible to study escape from broad shallow wells, narrow deep wells, and along phase paths with multiple metastable minima and saddle points. In addition, the curvature along the escape path in the well, which determines the plasma frequency, and the (negative) curvature at the saddle point, which affects the damping parameter, can be substantially different. This is in contrast to the RSJ model where the two frequencies are equal.

Since the barrier height in a dc SQUID potential can be changed at a fixed bias current, it is possible to tune the transition rate and switch the device between the thermal activation and MQT regime at a fixed temperature. In essence, one has a variable critical current in such a device. This capability is valuable for identifying the dominant transition mechanism and may be a crucial element for observing macroscopic quantum coherence.

The dc SQUID system also has various technical advantages over the single junction. A crucial issue in MQT measurement is the signature of MQT itself: a temperature-independent escape rate. If spurious noise is present in the measuring apparatus, the result would also be a temperature-independent escape rate. One has to ascertain that this "flattening" is due to MQT itself and not external transients. Since the switching current (potential barrier

height) in dc SQUIDs can be varied externally (Figure 2.6), one can fabricate a device such that the escape mechanism is thermal at the lowest temperature of our refrigerator, where the escape rate should still be temperature-dependent. This is an important check of the measurement apparatus and enables us to check for the presence of external noise.

Another advantage of a dc SQUID is that it enables us to obtain device parameters independently from the I-V characteristics and not rely solely on fits. For example, the modulation depth of the switching current vs. flux can be used to determine the inductance of the SQUID loop. There are also resonances in the I-V that yield the value of the device capacitance accurately.

Energy contours for a symmetric SQUID with $i = 0$ at $f = 0$ and $f = 1/2$ are shown in Figure 5.9. The case shown is for $\beta_L \ll 1$ for which the saddle point over which thermal escape occurs lies on a line between adjacent potential wells. At zero flux bias, this path is the line $\delta_1 = \delta_2$; an increase of the flux bias shifts the wells and saddles in the δ_1 - δ_2 plane. For larger values of β_L, the potential is more complicated. The saddle point becomes a local maximum while two new saddles are formed on either side. The escape rate must include the rates through each saddle. We therefore chose to perform our measurements on a low-inductance dc SQUID.

We have fabricated devices based on either Pb-alloy or Nb technology as outlined in chapter 4. The Pb junctions were window type with areas of 0.8 μm^2 separated by 2 μm by the lifting off of windows in an SiO insulating layer on top of the base electrode.

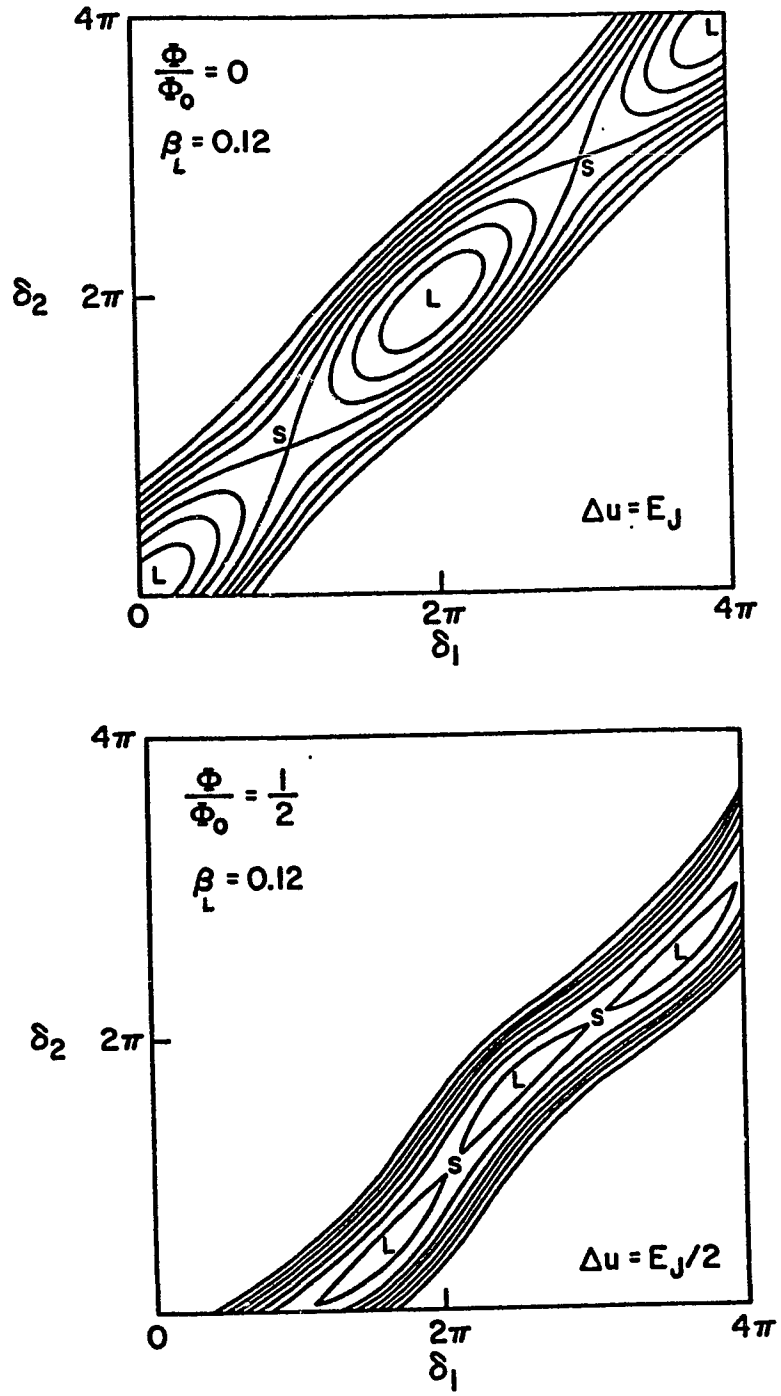

Figure 5.9 - Energy contours for a low β_L SQUID at two different values at flux bias. ΔU is the contour spacing.

Following ion-mill cleaning of the base electrode, and dc glow discharge oxidation, the counter electrode is deposited to complete the junction and close the inductance loop. The (magnetic) loop area of 0.2 μm^2 yields an inductance of 2.4 pH, as determined from the modulation depth. The capacitance of each junction is estimated to be 80 fF. This value is obtained from the dielectric constant of the insulators and the geometry of the device and agrees with resonance measurements. The Nb devices were similar in size and geometry, but had higher inducatnce values and lower critical currents.

We made measurements on various SQUIDs. The most interesting results were obtained from a symmetric Pb device with $2I_C$ = 107 μA and β_L = 0.12. For this device measurements were obtained at temperatures from 50 mK to 1.7 K and at five flux biases: f = 0, 1/4, 1/2, 3/4, 1. Theoretically, the potentials at f = 1, 3/4 should yield equivalent escape rates to those at f = 0, 1/4, respectively. The measurements at the former flux values enable us to determine the modulation of the single junction critical currents by the applied field and test for flux noise from the magnetic field source.

The escape rates were measured in the usual fashion by obtaining distributions of switching events. These are characterized by their first and second moments, <I> and σ, corresponding roughly to their peaks and widths. Figures 5.10, 5.11, 5.12 show the measured peaks and widths versus temperature for three different values of flux. The data at f = 1 and f = 3/4 are essentially the same as the f = 0 and f = 1/4 results as expected, aside from a small suppression of the single junction critical current by 12% at f = 1. This indicates

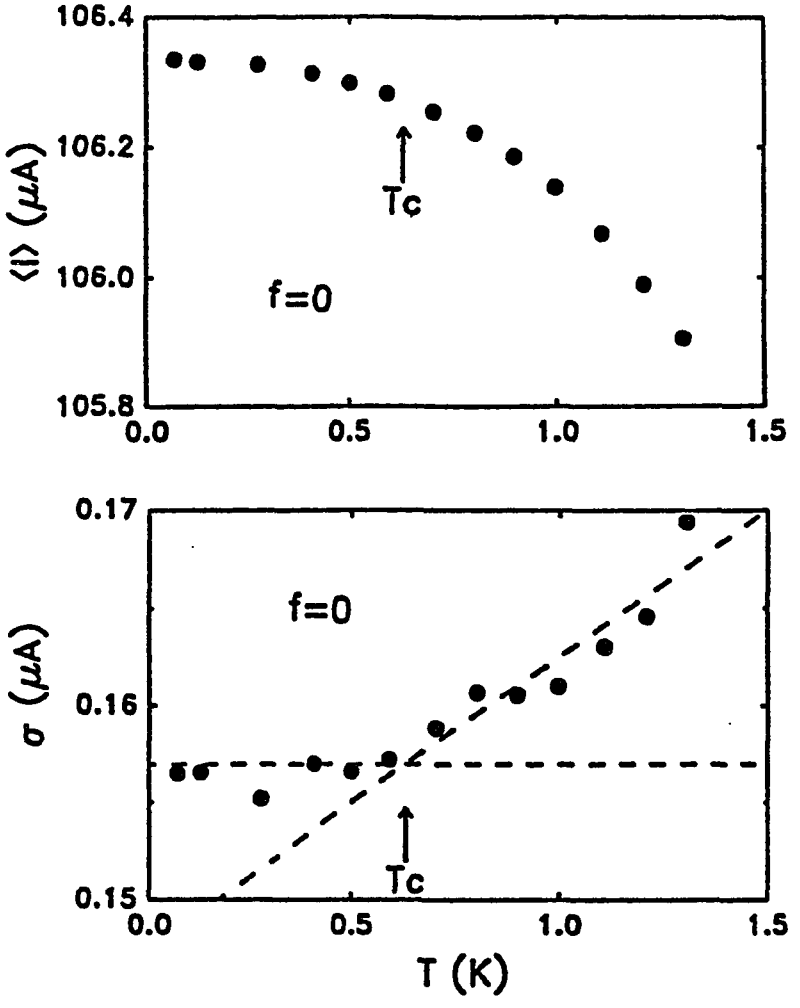

Figure 5.10 - First and second moments of the switching distributions at f = 0. T_c is the crossover temperature signifying MQT.

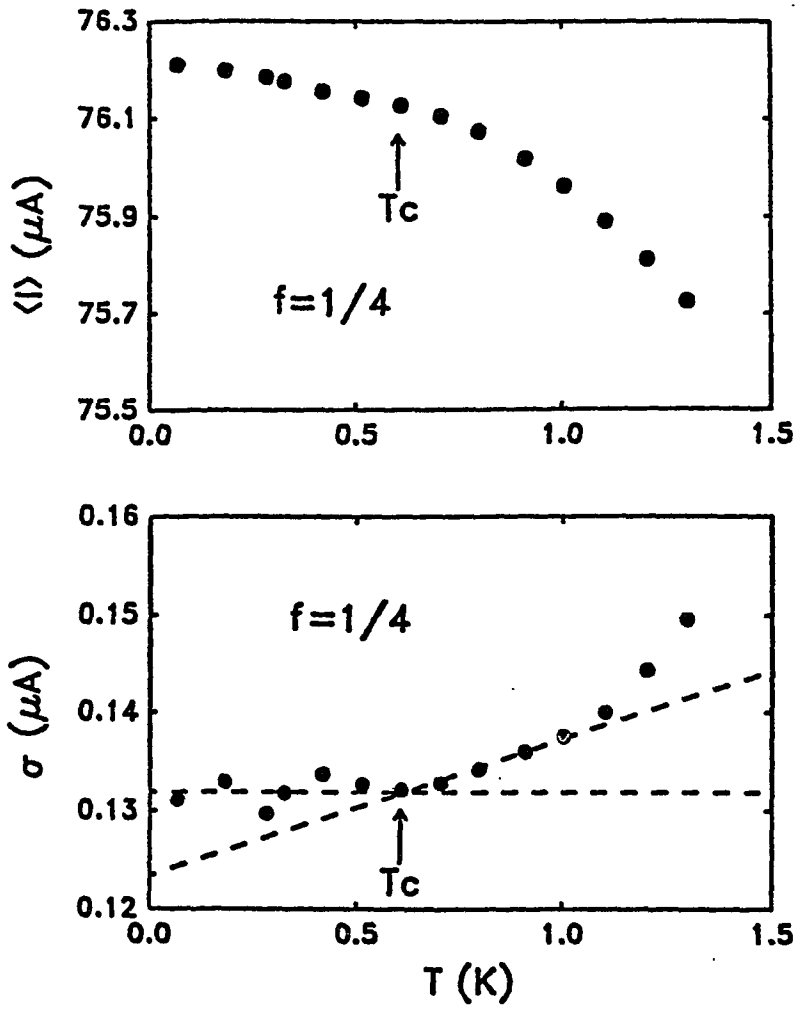

Figure 5.11 - First and second moments of the switching distributions at f = 1/4. T_C is the crossover temperature signifying MQT.

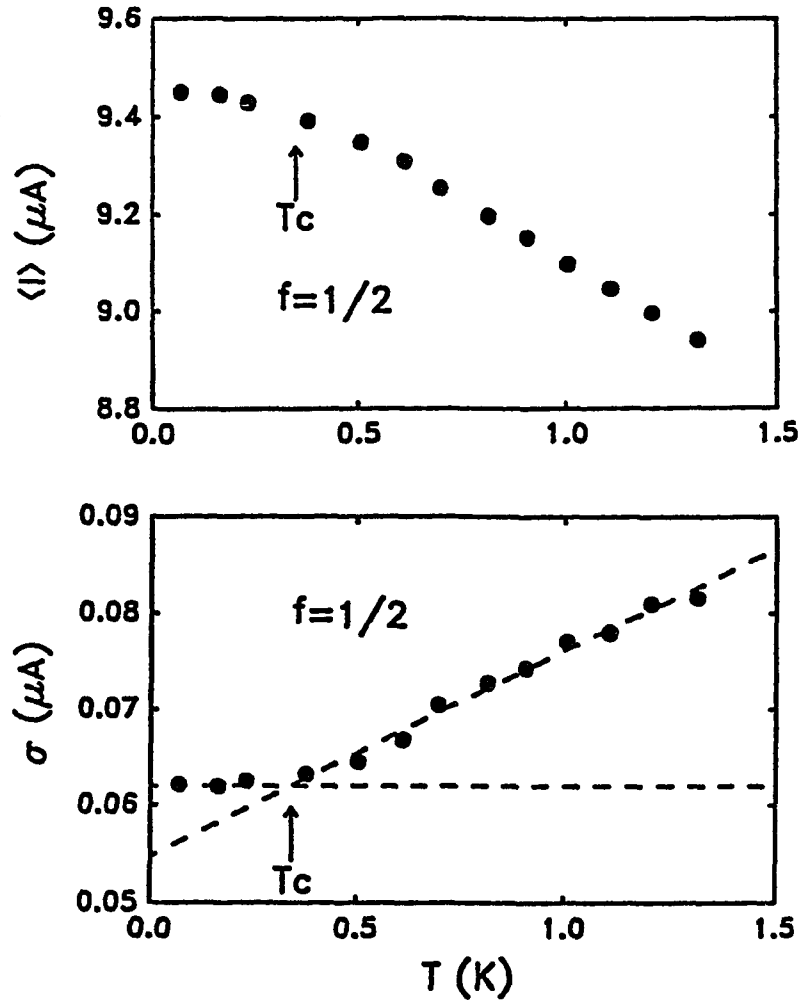

Figure 5.12 - First and second moments of the switching distributions at $f = 1/2$. T_c is the crossover temperature signifying MQT.

that external flux noise is not affecting the transition rate. We also note that the variation of the peaks and widths with temperature at f = 1/2 extends to below 100 mK, which puts an upper bound on the external noise from other sources. At each flux, the distribution width decreases roughly linearly as the temperature is lowered and flattens abruptly at the crossover temperature T_c. The peak increases and eventually also flattens, although the transition is substantially more rounded than our single junction data. This occurs because <I> is proportional to the transition rate, while σ is a measure of the variation of the rate with bias current and is not as sensitive to changes in the prefactor that scale with the bias current [62]. The temperature independence of <I> and σ is the signature for MQT from the zero-voltage state.

We have performed computer simulations to determine distribution peaks and widths as functions of temperature and flux bias for a two-dimensional thermal activation model given by eq. (3.5). Since the thermal activation rate is only weakly dependent on the damping, the thermodynamic critical current, I_c, is the only parameter in our system that is not independently determined and must be derived from a fit in this regime.

Surprisingly though, we are unable to fit our thermal results with any choice of I_c or any reasonable (or even unreasonable) adjustment of the other device parameters. The predicted temperature dependence (curve labelled TA in Figures 5.13, 5.14) is considerably greater than we observe. In the thermal activation model, the magnitude of the thermal transition is a strong function of the SQUID parameters,

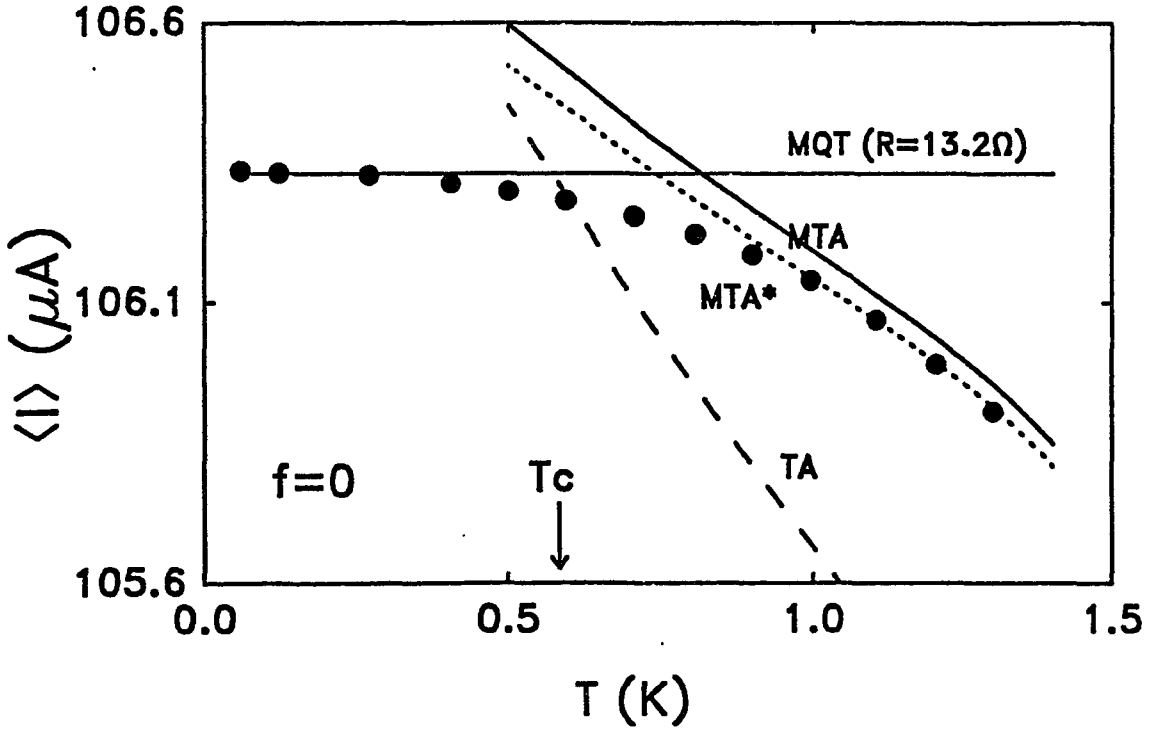

Figure 5.13 - Comparison of the first moment data at f = 0 with a two dimensional thermal activation model (TA) and a modified thermal activation model incorporating an enhanced barrier height without (MTA) and with (MTA*) quantum corrections to the thermal rate. Also plotted is the predicted MQT rate for the damping resistance indicated.

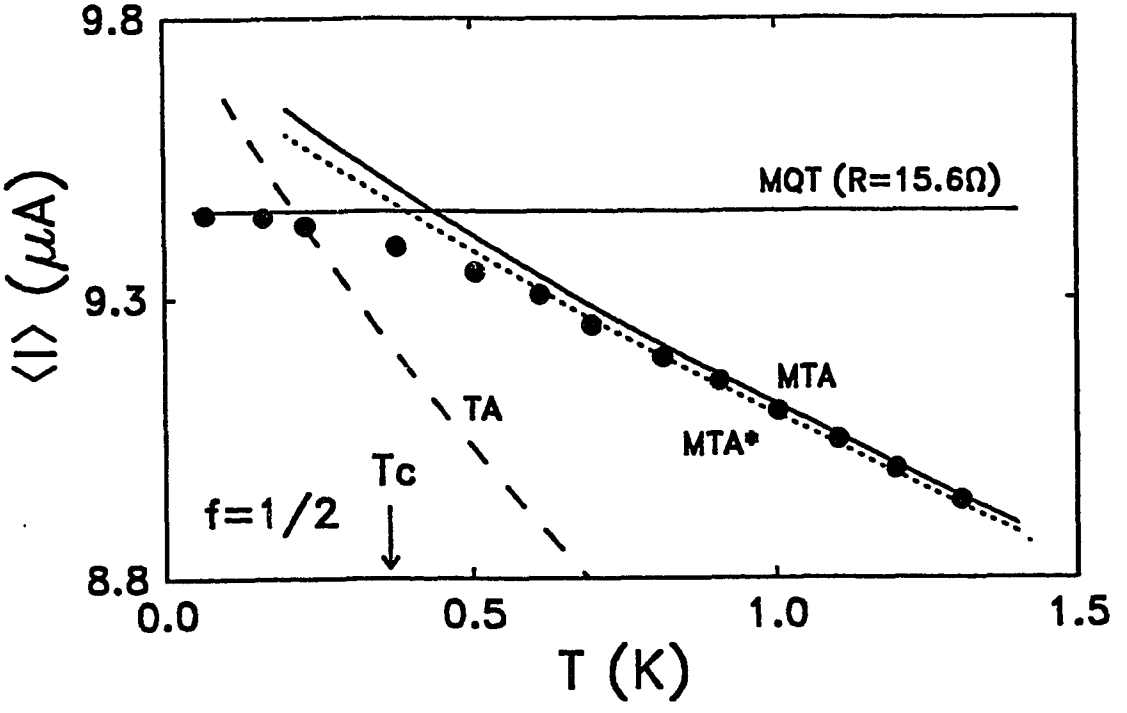

Figure 5.14 - Comparison of the first moment data at f = 1/2 with a two dimensional thermal activation model (TA) and a modified thermal activation model incorporating an enhanced barrier height without (MTA) and with (MTA*) quantum corrections to the thermal rate. Also plotted is the predicted MQT rate for the damping resistance indicated.

particularly I_C, but the slope versus temperature is fairly insensitive to parameter changes. Our results indicate that the thermal activation rate is significantly suppressed in the two-dimensional potential of the dc SQUID. In fact we are only able to model our data accurately by assuming that the barrier height by a factor of about 2.5. Using eq. (3.5) with an enhanced barrier height $\Delta U^* = 2.5\Delta U$ we obtain the fit labelled MTA in figures 5.13 and 5.14. With this enhanced barrier height, we are able to fit our thermal results accurately well above T_C for all bias fluxes and extract a value for I_C. We note that previous measurements of thermally induced transitions between different zero voltage vortex states in Josephson interferometers have shown good agreement with the thermal activation model [63], although the parameters of these devices are significantly different than ours. We emphasize that we have no direct justification for such an enhancement and our factor of 2.5 is derived solely on the basis of our fit. However, we conjecture two possible scenarios that could lead to an enhancement of the barrier height.

Recently, Suhl [19] has shown that it may be possible for the thermal activation rate in a multi-dimensional potential system to be significantly reduced under certain conditions. At present, we are not sure if the criteria he sets applies to our potential.

A more likely explanation for what we observe is that the effect is due to the energy quantization of the (flux) mode orthogonal to the escape direction. Since the SQUID has a low inductance, its orthogonal frequencies are higher than the parallel frequencies

(Figure 5.15); the zero point energy of the orthogonal mode is correspondingly larger. The thermal activation model is only expected to apply in a regime where the particle in the well has a thermal energy distribution. This requires that the number of energy levels in the well be large and that they be populated according to a Boltzman distribution. In Figure 5.16 the number of energy levels in the well for both the parallel and orthogonal frequency modes is plotted versus temperature at the bias current at which the escape occurs. The transition to MQT occurs when there is approximately one level in the direction along the escape path. However the energy corresponding to the orthogonal frequency mode exceeds the barrier height significantly. This implies that this mode is essentially frozen into a ground state and would not exhibit a thermal distribution. Consequently, we might not expect the system to obey a Boltzman thermal activation factor. If this picture is valid, we would then expect the system to revert to the Kramers' form only when the orthogonal mode also became thermal. For the case of $f = 0$, this would entail taking measurements above 2K while for the $f = 1/2$ case, the measurements would have to be done above 4K. We have some circumstantial evidence that this model is essentially correct from the curvature of the <I> versus T plots in figure 5.13. Here we see that the slope of the line is approaching that of the TA model gradually since we are slowly approaching the temperature where the orthogonal mode also becomes thermal. Howewver, there is no such curvature for the $f = 1/2$ case since we are not close to this temperature. It is not possible to take measurements at temperatures

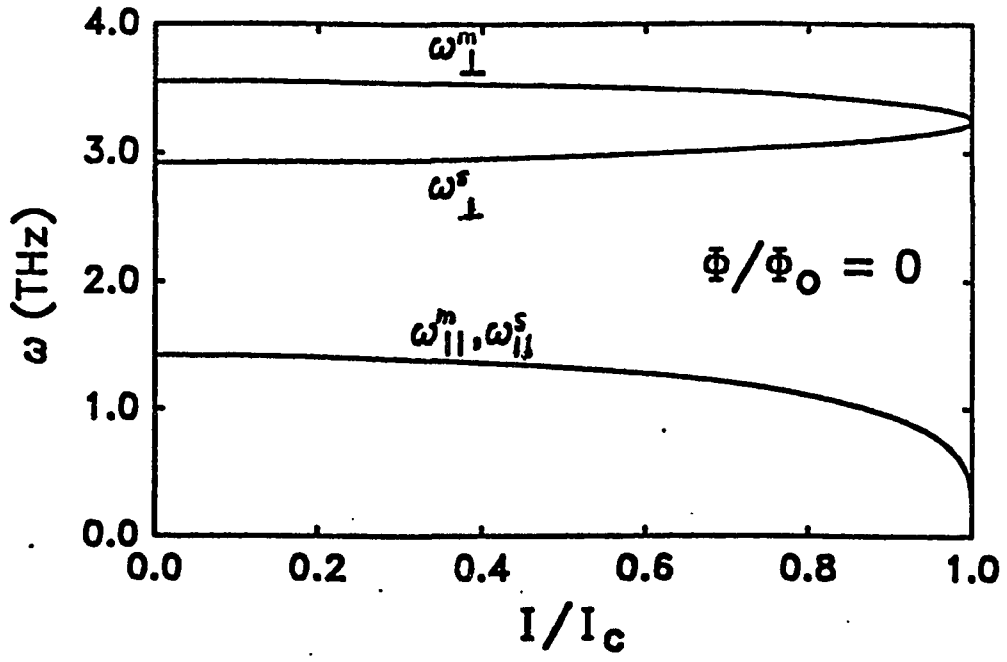

Figure 5.15 - Dependence of the parallel and orthogonal frequency modes at the local minimum and saddle point on the bias current at f = 0.

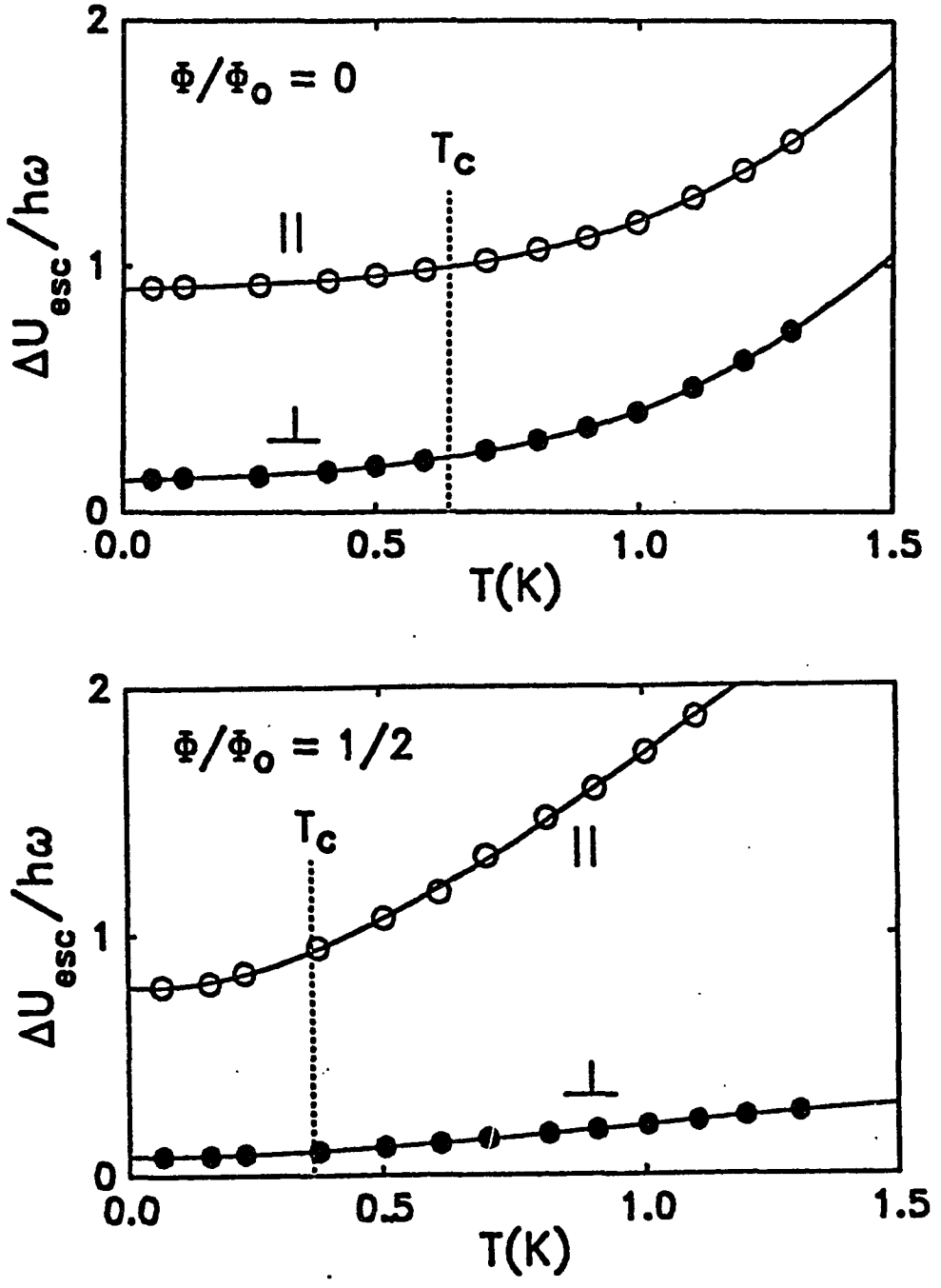

Figure 5.16 - Number of energy levels in the well in the parallel and orthogonal directions as a function of temperature for f = 0 and f = 1/2.

much above 1.5 K because the change in superconducting gap in Pb starts to become an overwhelming effect and would swamp the fluctuation effects we are measuring.

In the far quantum regime, things appear to be better behaved. From the calculations performed by Chen [26], we expect the single junction quantum escape rate results to be a good approximation for our two-dimensional potential. With this model and using the usual unenhanced barrier height, we find good agreementwith the aymptotic peak value for an effective damping resistance of 15.6 Ω and a slightly lower value (13.2 Ω) at f = 1/2. If the damping correction is neglected, the predicted MQT peak transition current is 105.2 μA at f = 0 and 8.8 μA at f = 1/2. Both of these are well below the observed value. This damping number is comparable to the normal state resistance of our SQUID, in agreement with previous work on unshunted devices.

The moderate damping also couples thermal and quantum processes and contributes to the rounding of the peak data in the crossover region. We have used a one-dimensional model to include the leading quantum corrections to the thermal rate above T_c in our simulations. These do yield an improved fit (dotted line labelled MTA* in Figures 5.13, 5.14) and may also account for the temperature dependence of the peak data below T_c. A full multi-dimensional quantum treatment is required to include these effects over the full crossover region.

In order to further elucidate the descrepancy in our thermal activation result, we recently performed escape rate measurements on a high-quality Nb device that had both a single junction and various

SQUIDs on one substrate. Although we had previously measured thermal escape rates in a single junction and had obtained good agreement with theory, we decided to again perfrom these measurements to ensure that the results we were observing were not due to an experimental error. Not surprisingly, we again obtained good agreement with the predictions of Kramer's one-dimensional thermal activation model.

We also performed thermal escape rate measurements on a Nb SQUID on the same substrate. The device had a lower critical current and higher inductance than the Pb-alloy SQUID. Consequently, the plasma frequencies in the two mode are more closely matched than the previous device. Measurements on this SQUID also yielded results that agreed well with the two-dimensional thermal activation model. Since all the measurements were done in identical experimental conditions, it is difficult to explain the descrepancy we observed in our earlier measurements as being caused by experimental error.

At the time of writing of this thesis, we received a preprint [64] describing an experiment in which thermal escape rates were measured in a two-dimensional potential. The plasma frequencies in this device are substantially lower than ours and consequently, the zero-point energy of both modes is lower than the barrier height. Not surprisingly, the thermal activation rates agree well with the theoretical predictions. We are currently performing more experiments to try to shed more light on this phenomena and test some of our hypotheses that may possibly explain this descrepancy.

Chapter 6

FUTURE DIRECTIONS

There are numerous areas in this field where further research is required. The dissipation question is extremely important and far from being resolved. Not only is the damping issue important for future quantum coherence experiments, it will also lead to a better understanding of the dynamics of Josephson junctions and the frequency dependence of the intrinsic resistance.

Dissipation can also be viewed to give a satisfactory explanation of a quantum measurement process. The collapse of a quantum system into an eigenstate during a measurement can be regarded as imposing heavy damping on the system. Although this point of view does not clarify the reason for the initial existence of linear superposition of states, it at least removes some of the incomprehensible mysticism of quantum meaurement theory.

The interaction of modes in multi-dimensional potentials is also an interesting issue and hardly any theoretical work exists at present time to model this situation. Since one mode in our system was frozen into a quantized level, future escape rate calculations attempting to explain our data will probably have to include possible induced non-equilibrium effects of this mode on the thermal bath.

There many other fascinating and unexplored areas in the two-dimensional potentials of dc SQUIDs. For instance, in high β_L devices, there exists the possibility of observing quantum

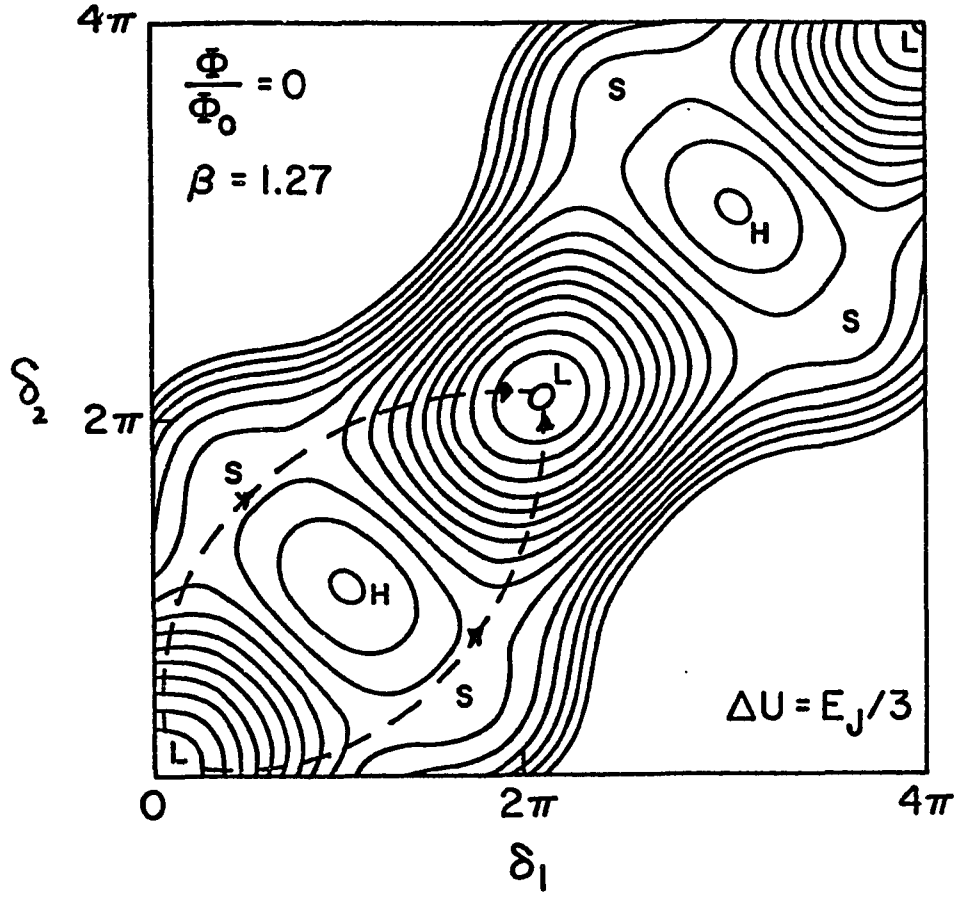

Figure 6.1 - High β_L SQUID potential in which it may be possible to observe macroscopic quantum interference effects. The dashed line indicates the two escape paths.

interference effects between the two escape paths (Figure 6.1). Classically, the escape rate for the two paths should be the sum of the escape rate for each path,

$$\Gamma_c = \Gamma_1 + \Gamma_2 \ . \tag{6.1}$$

However, because of interference effects between the two paths, the quantum escape rate will be larger,

$$\Gamma_q = \Gamma_1 + \Gamma_2 + 2\sqrt{\Gamma_1 \Gamma_2} \ . \tag{6.2}$$

Experimentally, one would measure the escape rate at zero flux bias. Then by applying a small flux, the barrier height of one of the saddles would become larger than the other. Since the rate is exponentially dependent on the barrier height, this would result in one path being effectively closed. Thus there should be a difference of a factor of four between the two rate measurements.

There are other experimental scenarios that one could study as well. For example by inducing an asymmetry in the inductance, the length of the two paths will become different. Then by measuring the rate as a function of bias current, one might be able to see oscillations of the rate when the two paths interfere constructively and destructively. The possibilities are endless!

6.1 Concluding Remarks

I would like to conclude this thesis with some personal thoughts regarding this fascinating subject. I think the main reason why fundamental quantum mechanics and especially quantum measurement theory no longer obtains the attention it deserves is because this

theory is installed into a physicist's learning process with a zeal almost approaching that of religion. We are so consistently taught not to question the subject that I believe most physicists today do not know what exactly is the paradox in the Schroedinger cat experiment. A clear example of this fervor not to question is a commentary by two emminent physicists in a recent issue of Physics Today [65]. In it we are told that the whole question of the Schroedinger experiment and macroscopic quantum mechanics is not only meaningless but also foolish. As I read the article with a sense of despair and disgust, I came across one hidden sentence that in essence refuted their whole argument. This sentence admitted somewhat hesitantly that indeed it is possible to study such effects in Josephson devices. The issue is not what happens when quantum mechanics is applied to an infinitely complicated system such as a cat, but rather the inherent uncertainties that quantum theory demands. Had Schroedinger known about Josephson devices, I believe it is likely he would have used them in his paradox.

Fortunately, there is some hope. It was delightful to read the backlash produced in response to this article. There is still a brave and vocal minority who are willing to question quantum authority.

REFERENCES

1. A. J. Leggett, Prog. Theor. Phys. 69, 80 (1980).

2. A. J. Leggett in Percolation, Localization, and Superconductivity, eds. A. M. Goldman and S. Wolf, NATO Advanced Studies Institute Series B, Vol. 109, Plenum, New York (1984).

3. J. S. Bell, Speakable and Unspeakable in Quantum Mechanics, Cambridge Press, Cambridgeshire (1987).

4. A. O. Caldeira and A. J. Leggett, Ann. Phys. (NY) 149, 374 (1983).

5. M. Tinkham, Introduction to Superconductivity, Krieger Publ. Co., New York (1975).

6. P. G. DeGennes, Superconductivity of Metals and Alloys, Benjamin Inc. New York (1966).

7. B. D. Josephson, Phys. Lett. 1, 251 (1962).

8. W. C. Stewart, Appl. Phys. Lett. 12, 277 (1969).

9. D. E. McCumber, J. Appl. Phys. 39, 3113 (1968).

10. A. Barone, and G. Paterno, Physics and Applications of the Josephson Effect, Wiley-Interscience, New York (1982).

11. T. Van Duzer and C. W. Turner, Principles of Superconducting Devices and Circuits, Elsevier, New York (1981).

12. J. Clarke in Superconductor Applications: SQUIDs and Machines, eds. B. Schwartz and S. Foner, Plenum, New York (1977).

13. C. D. Tesche, J. Low Temp. Phys. 29, 301 (1977).

14. H. A. Kramers, Physica (Utrecht) 7, 284 (1940).

15. M. Buttiker, E. Harris, and R. Landauer, Phys. Rev. B 28, 1268

(1983).

16. R. Landauer and J. Swanson, Phys. Rev. 121, 1668 (1961).

17. E. Turlot et. al., Phys. Rev. Lett. 62, 1788 (1989).

18. P. B. Visscher, Phys. Rev. B 14, 347 (1976).

19. H. Suhl, Phys. Rev. Lett. 60, 473 (1988).

20. H. C. Brinkman, Physica (Utrecht) 22, 149 (1956).

21. E. Ben-Jacob et. al., J. Appl. Phys. 54, 6533 (1983).

22. C. D. Tesche, J. Low Temp. Phys. 44, 119 (1981).

23. Z. Schuss, SIAM Rev. 22, 119 (1980).

24. A. O. Caldeira and A. J. Leggett, Phys. Rev. Lett. 46, 211 (1981).

25. A. Schmidt, Annals of Physics 170, 333 (1986).

26. Y. -C. Chen, J. Low Temp. Phys. 65, 133 (1986).

27. R. F. Voss and R. A. Webb, Phys. Rev. Lett 47, 265 (1981).

28. M. H. Devoret, J. M. Martinis, and J. Clarke, Phys. Rev. Lett. 55, 1908 (1984).

29. M. H. Devoret, J. M. Martinis, D. Esteve, and J. Clarke, Phys. Rev. Lett. 53, 1260 (1984).

30. J. M. Martinis, M. H. Devoret, and J. Clarke, Phys. Rev. Lett. 55, 1543 (1985).

31. A. O. Caldeira and A. J. Leggett, Ann. Phys. (NY) 149, 374 (1983).

32. L. D. Chang and S. Chakravarty, Phys. Rev. B. 29, 130 (1984).

33. L. D. Chang and S. Chakravarty, Phys. Rev. B. 30, 1566(E) (1984).

34. M. H. Devoret et. al., Phys. Rev. B 36, 58, (1987).

35. S. Washburn, R. A. Webb, R. F. Voss, and S. M. Faris, Phys. Rev. Lett. 54, 2712 (1985).

36. Y. -C. Chen, M. P. A. Fisher, A. J. Leggett, J. Appl. Phys. 64, 3119 (1988).

37. J. R. Kirtley et. al. Phys. Rev. Lett. 61, 2372 (1988).

38. H. Grabert, P. Olschowski, and U. Weiss, Phys. Rev. B 36, 1931 (1987).

39. H. Grabert and U. Weiss, Phys. Rev. Lett. 53, 1787 (1984).

40. D. B. Schwartz, B. Sen, C. N. Archie, and J. E. Lukens, Phys. Rev. Lett. 55, 1547 (1985).

41. A. Fathimula, J. Vac. Sci. Tech. B3, 25, (1982).

42. G. J. Dolan, Appl. Phys. Lett. 31, 337 (1977).

43. S. K. Lahiri, S. Basavaiah, and C. J. Kircher, Appl. Phys. Lett. 36, 334 (1980).

44. S. K. Lahiri and S. Basavaiah, J. Appl. Phys. 49, 2820 (1978).

45. S. Basavaiah, M. Murakami, and C. J. Kircher, J. Phys. (Paris) 39, C6-1247 (1978).

46. H. R. Kauffman, Fundamentals of Ion-Source Operations, Commonwealth Scientific Corp., Alexandria, Va. (1984).

47. E. E. Latta and M. Gasser, J. Appl. Phys. 54, 1115 (1983).

48. A. W. Kleinsasser and R. A. Buhrman, Appl. Phys. Lett. 37, 841 (1980).

49. H. Kroger, L. N. Smith, and D. W. Jillie, Appl. Phys. Lett. 39, 280 (1981).

50. M. Gurvitch, M. A. Washington, and H. A. Huggins, Appl. Phys. Lett. 42, 472 (1983).

51. J. M. Rowell, M. Gurvitch, and J. Geerk, Phys. Rev. B 24, 2278 (1981).

52. S. Morohashi and S. Hasuo, J. Appl. Phys. 61, 4835 (1987).

53. K. Kuroda and M. Yuda, J. Appl. Phys. 63, 2352 (1988).

54. F. Sharifi, K. Stawiasz, D. J. Van Harlingen, and J. Zmuidzinas, submitted to Appl. Phys. Lett.

55. W. H. Thornton, J. Taback, and D. W. Hoffman, Thin Solid Films 64, 111 (1979).

56. T. A. Fulton and L. N. Dunkelberger, Phys. Rev. B 9, 4760 (1974).

57. D. Rogovin and D. J. Scalapino, Annals of Physics 86, 1 (1974).

58. A. F. Hebard and S. Nakahara, Appl. Phys. Lett. 41, 1130 (1982).

59. A. T. Fiory and A. F. Hebard, Physica 135B, 124 (1985).

60. F. Sharifi, J. L. Gavilano, and D. J. Van Harlingen, Phys. Rev. Lett. 61, 742 (1988).

61. F. Sharifi, J. L. Gavilano, D. J. Van Harlingen, IEEE Trans. Mag. MAG-25 (1989).

62. D. B. Schwartz et. al. Phys. Rev. Lett. 55, 1547 (1985).

63. M. Naor, C. D. Tesche, and M. B. Ketchen, Appl. Phys. Lett. 41, 202 (1982).

64. S. Han, J. LaPointe, J. Lukens, preprint

65. H. Feshback and V. F. Weiskopf, Physics Today 41 (10), 9 (1988).

VITA

Fred Sharifi was born on September 9, 1961 in Iran. He graduated from the American Community School in Buenos Aires, Argentina in 1978. He received his B.S. in Physics in 1982, graduating Magna Cum Laude and obtained his M.S. the following year. In 1983, he received the Scott Anderson Award for teaching. During the 1988-1989 academic year, he was a University Fellow.